

Direct observation of vortex liquid droplets in the iron pnictide superconductor $\text{CaKAs}_4\text{Fe}_4$ at 0.5T_c

Óscar Bou Marqués,¹ Jose A. Moreno,¹ Pablo García Talavera,¹ Mingyu Xu,^{2,3,*} Juan Schmidt,^{2,3,4} Sergey L. Bud'ko,^{2,3} Paul C. Canfield,^{2,3} Isabel Guillamón,¹ Edwin Herrera,¹ and Hermann Suderow¹

¹*Laboratorio de Bajas Temperaturas, Departamento de Física de la Materia Condensada, Instituto Nicolás Cabrera and Condensed Matter Physics Center (IFIMAC), Unidad Asociada UAM-CSIC, Universidad Autónoma de Madrid, E-28049 Madrid, Spain.*

²*Ames National Laboratory, Iowa State University, Ames, Iowa 50011, USA*

³*Department of Physics and Astronomy, Iowa State University, Ames, Iowa 50011, USA*

⁴*Departamento de Física, FCEyN, Universidad de Buenos Aires, Buenos Aires 1428, Argentina*

Type-II superconductors under magnetic fields are in a quantum coherent non-dissipative state as long as vortices remain pinned. Dissipation appears when vortices depin, eventually driven by thermal fluctuations. This can be associated to a melting transition between a vortex solid and a vortex liquid. This transition is almost always observed very close to T_c when probed by macroscopic experiments. However, it remains unclear how the vortex solid responds to thermal fluctuations at the scale of individual vortices far from the melting transition. Here we use scanning tunneling microscopy (STM) to visualize vortices in $\text{CaKAs}_4\text{Fe}_4$ ($T_c \approx 35$ K). We find vortex liquid droplets—localized regions in space where vortices strongly fluctuate due to thermal excitation—at temperatures as low as 0.5T_c . Our results show that the onset of dissipation at the local scale occurs at temperatures considerably below T_c in type-II superconductors.

INTRODUCTION

In type II superconductors the magnetic field can penetrate in the material in the form of superconducting vortices. Inside the vortex core the superconducting pair wavefunction is suppressed on the scale of the superconducting coherence length ξ . In a clean superconductor vortices arrange themselves in an ordered lattice [1]. But real materials rarely maintain this ordered ideal vortex solid. Vortex cores threading regions with crystalline defects, for example, have a smaller core free energy and such vortices tend to remain pinned to the defected regions. This, combined with the variations in the intervortex interactions as a function of temperature and magnetic field and with thermal fluctuations, eventually leads to a phase transition between a vortex solid and a vortex-liquid [2–7]. Vortices are essentially mobile in the vortex liquid phase, which may produce dissipation under the application of an infinitesimal perturbation as for example, a small current [8–11].

The relevance of thermal fluctuations for a certain superconductor can be described by the Ginzburg-Levanyuk number G_i [12, 13]. G_i compares the critical temperature T_c with the free energy of the superconductor in a volume defined by the coherence length ξ , $G_i = \frac{k_B T_c}{H_c^2 \xi^3}$ (for isotropic superconductors, where H_c is the thermodynamic critical field and k_B Boltzman's constant). G_i is directly related to thermally induced motion of vortices, which is more relevant for higher values of G_i [2, 3, 7, 14, 15]. G_i can be also related to the temperature and field range presenting a vortex liquid

phase [16]. The vortex liquid phase is practically absent in low T_c superconductors with $G_i \approx 10^{-7}$ and occurs in a temperature range a few % below T_c in cuprate superconductors with $G_i \approx 10^{-3} - 10^{-2}$.

The melting process of the vortex solid in high magnetic fields, where the intervortex separation is larger but of the order of ξ , has been studied by macroscopic measurements including specific heat or magnetization [17–21], microscopic but spatially averaged techniques as small angle neutron scattering [22–24], and through direct visualization in real space such as scanning tunneling microscopy (STM) [25–39]. Other spatially resolved techniques as Magnetic Force Microscopy mostly address the range of small magnetic fields and intervortex separations much larger than ξ [40]. STM allows to image individual vortices in the field range which is mostly used in applications [8, 9, 41]. Often, the electronic density of states at the Fermi level inside vortex cores is much larger than the density of states outside vortex cores (the latter is, for low fields, similar to the one obtained in zero field superconducting density of states measurements). By making maps of the zero bias tunneling conductance, which is proportional to the Fermi level electronic density of states, many individual vortices are imaged in a large range of magnetic fields [25–38]. However, vortex studies with STM have been mostly restricted to superconductors with very small G_i . Measurements of the vortex phases as a function of temperature in high T_c cuprate superconductors with large G_i show mostly vortex solid phases with different degrees of thermally induced disorder [42]. The observation of melting remains challenging, because the density of states in and around vortices is intricate and difficult to follow with temperature [43–46].

Owing to their relatively large T_c and small coherence length ξ , iron pnictide superconductors provide enhanced fluctuations and a relatively large vortex liq-

* Currently at: Department of Chemistry, Michigan State University, East Lansing, Michigan 48824, USA

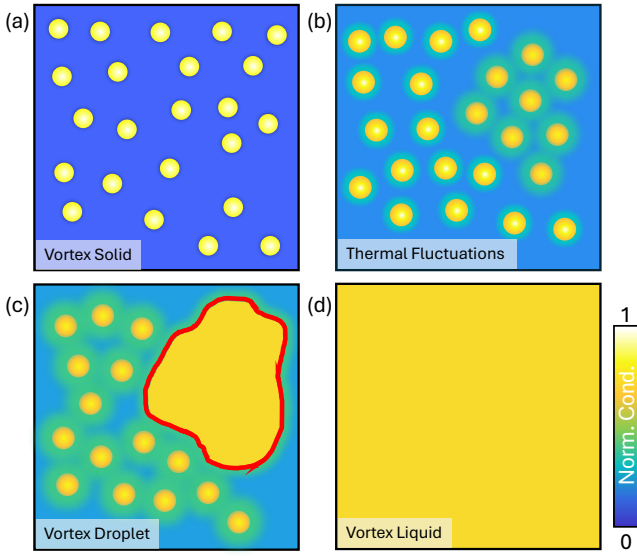


FIG. 1. Schematic representation of vortex solid and liquid phases. (a) At low temperatures, the vortices are pinned and eventually form a disordered solid. The superconducting state (dark blue) is clearly distinguished with respect to the normal state at the center of the vortex core (white). (b) As the temperature rises, vortices begin to move, hopping between different positions. Vortex motion leads to fluctuations in the vortex positions which are much faster than our measurement time, resulting in an apparent increase in the vortex core size (the time-averaged density of states is represented by the green halo). (c) In certain areas we eventually observe “vortex liquid droplets” (large yellow area marked by the red line). These droplets coexist with a vortex solid. (d) Close to the critical temperature, T_c , of the superconductor, we observe a vortex liquid spanning large fractions of the field of view. The vortex liquid phase consists of large areas with a spatially uniform tunneling conductance which is below the tunneling conductance at high values, evidencing the presence of a superconducting gap.

uid range in the temperature-magnetic field phase diagram [14, 16]. Critical temperatures as high as $T_c = 35$ K occur in the stoichiometric material $\text{CaKFe}_4\text{As}_4$, which also presents a coherence length ξ_{ab} below 2 nm [47–50]. With $G_i \approx 10^{-4}$, a well defined density of states inside vortex cores[51], and clear a-priori knowledge of most relevant pinning centers (CaFe_2As_2 and KFe_2As_2 intergrown layers [52–61]), $\text{CaKFe}_4\text{As}_4$ arises as an excellent system to study thermal fluctuations at the scale of individual vortices. Here we address the vortex solid and liquid phases of $\text{CaKFe}_4\text{As}_4$ using STM and unveil vortex liquid droplets appearing locally well below T_c .

It is important to realize that STM measures at time scales of several tens of minutes. In the presence of thermal fluctuations, the tunneling conductance is acquired at a single point and is the result of the time average over a vortex changing its position continuously below the tip. The tip rests on top of a vortex generally for a few seconds (depending on the vortex density and image

size). Except at locations with exceptionally slow dynamics (discussed below), taking tunneling conductance measurements as a function of time at a single vortex generally does not provide a significant time dependent signal, suggesting that the time scale for most fluctuations is well above the fastest measurement time scale, determined by the acquisition bandwidth (of about 10 kHz) [62]. If the amplitude of fluctuations is no bigger than the vortex core, we see perfectly defined cores just as shown in Fig. 1(a). When fluctuations are larger than the vortex core size, the tunneling conductance map shows an apparent increase in the core size, as schematically represented in Fig. 1(b) and in the portion of (c) showing the vortex solid. We identify the vortex liquid when we do not observe individual vortices at locations where we observe individual vortices at lower temperatures. We consider that areas presenting a spatially uniform zero bias tunneling conductance and which are larger than three times the average intervortex distance are in the vortex liquid state. In the vortex liquid, Fig. 1 (d) and the portion of (c) showing the vortex liquid, we observe a tunneling conductance at zero bias below its value at high bias (schematically shown by the yellow color, instead of white for the normal phase, in Fig. 1) [28–31].

RESULTS

In Fig. 2(a-e), we show a characteristic example of zero bias conductance maps at different temperatures within the same field of view. At 10 K (Fig. 2(a)) we observe individual vortices all over the image. Intervortex distance follows the prediction for the triangular Abrikosov vortex lattice, as shown at lower temperatures in Ref. [51]. There are also features in the vortex maps where the tunneling conductance forms lines with a conductance slightly below, but close to the normal phase value. These linear features can be associated with lines observed in the STM topography, see Supplementary Information Section I and Supplementary Fig. 1. At 15 K and at higher temperatures (Fig. 2(b-e)) we observe that there are areas, which we call vortex liquid droplets, where vortices merge into increasingly larger patches, within the areas marked by a red line. These areas coexist with the disordered vortex solid, where we can still resolve individual vortices. Vortex liquid droplets are observed at temperatures as small as 0.5 T_c . At the highest temperature, 30 K (T_c at this field is of about 32 K as obtained from resistivity [50]), vortex liquid areas encompass nearly half the whole field of view.

It is important to plot the normalized tunneling conductance in different parts of the field of view as a function of the temperature (Fig. 2(f)). The tunneling conductance $\sigma(V)$ is given by $\sigma(V) = \int dE N(E) \frac{df(E-eV)}{dE}$, where $N(E)$ is the density of states, $f(E)$ the Fermi function and E the energy. $N(E)$ for $\text{CaKFe}_4\text{As}_4$ has been discussed before and is understood as a modified BCS density of states described in Refs. [49, 51, 63]. The zero

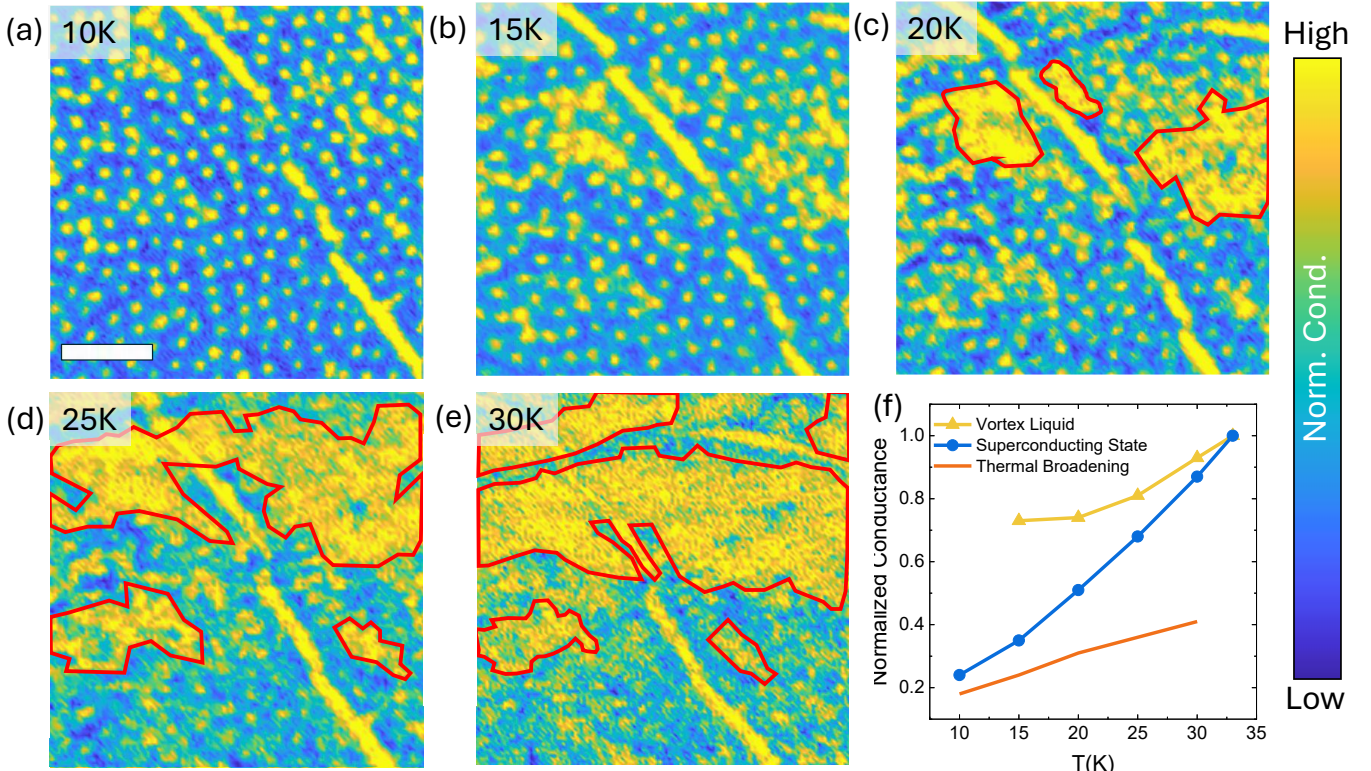


FIG. 2. **Direct observation of vortex liquid droplets well below T_c in $\text{CaKAs}_4\text{Fe}_4$.** In (a-e) we show maps of the zero bias tunneling conductance for different temperatures and at 10 T, in approximately the same field of view. Linear defects found in the surface of the sample lead to the roughly diagonal yellow lines shown in the maps (more information in the Supplementary Information Section I and Supplementary Figures 1. and 2; maps at other temperatures and magnetic fields are commented and provided in the Supplementary Information Section III and in the Supplementary Figure 4). At higher temperatures we mark with red contours the areas where we do no longer identify isolated vortices in the tunneling conductance maps. In these areas, the tunneling conductance is still well below that of the normal phase. The white scale bar in panel (a) corresponds to 40 nm. The color scale corresponds to slightly different conductance values in each figure, to maximize contrast. To discuss the value of the conductance in (a-e) we show in (f) the tunneling conductance at zero bias normalized to its high bias value versus temperature, taken at different positions. Lines connect points and are guides to the eye. We show the tunneling conductance taken in between vortices (blue areas in (a-e)) as blue circles. The change induced by the temperature smearing in the zero bias tunneling conductance is shown as an orange line. We also show as yellow triangles the tunneling conductance inside the vortex liquid droplets (average over areas within the red lines in a-e).

energy density of states is zero, except on impurities or defects [49, 51]. With increasing temperature, the superconducting gap decreases, and there is an enhanced $\sigma(V=0)$ due to the temperature smearing by the Fermi function. Its derivative, $\frac{d\sigma(E-eV)}{dE}$, changes from close to a δ function at absolute zero to a smeared peak with increasing temperature. The temperature induced increase in the zero bias tunneling conductance $\sigma(V)$ is shown by the orange line in Fig. 2(f). This corresponds to the temperature induced reduction of the contrast in observing vortices by measuring the tunneling conductance. We see however that the temperature variation of the zero bias tunneling conductance in between vortices (blue circles in Fig. 2(f)) is much stronger. This is due to thermally induced vortex core overlap. We discuss this with more detail in the Supplementary Information Section II and

Supplementary Figure 3 (maps taken at different temperatures and magnetic fields are shown in the Supplementary Information Section III and in the Supplementary Figure 4). Within the vortex liquid droplets, the tunneling conductance at zero bias is very different from the one in between vortices and also increases with temperature (yellow triangles in Fig. 2(f)). The zero bias tunneling conductance remains always below the normal phase value, evidencing the motion of vortices inside the liquid droplets.

We note that the liquid vortex droplets are formed at low temperatures in areas which are well separated from the linear defects (Fig. 2(b)). At higher temperatures (Fig. 2(e)), the vortex liquid droplets join the linear features in the tunneling conductance maps. We find that vortex liquid droplets preferentially form at areas where vortices present enhanced fluctuations at low tempera-

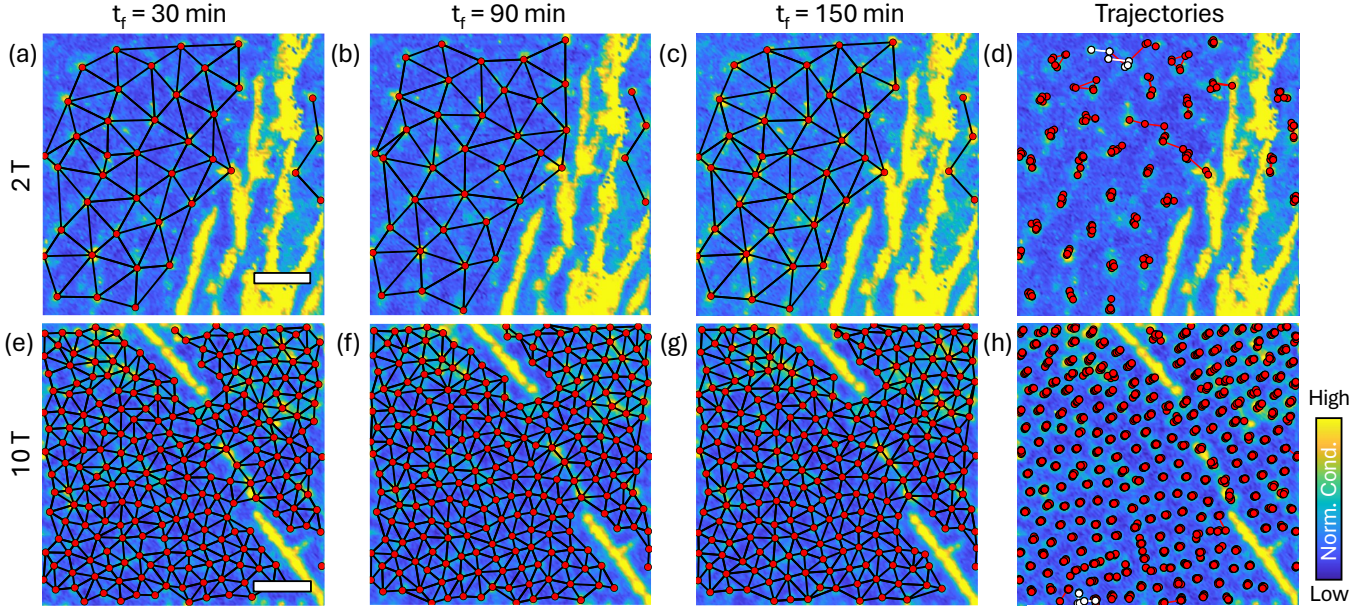


FIG. 3. Thermal fluctuations of vortices. In (a-c) and in (e-g) we show zero bias tunneling conductance maps acquired sequentially at, respectively, 2 T and 10 T. Each map has been taken in half an hour, and the field of view remains the same at each magnetic field. Vortex positions are marked by red circles. The black lines join nearest neighbour vortices, obtained by triangulation. In (d,h) we superimpose red circles united by a red line for each magnetic field ((d) for 2 T and (h) for 10 T) on the first zero bias tunneling conductance map of the sequence. These circles and red lines mark the trajectory of each vortex in the sequence. We see that most vortices remain at the same position. However, a few vortices have moved. For example, the vortices marked in white in the top central part of (d), or at the bottom center in (h), are the vortices in each case that present the largest displacement in the field of view. Note that the largest displacement is much larger at 2 T than at 10 T. In total, we acquired six consecutive images at each magnetic field. White bars in (a) and (e) correspond to 40 nm.

tures.

To explore the role of pinning in the melting process in more detail, we now discuss zero bias conductance maps taken consecutively at a fixed temperature and magnetic field. In Fig. 3, we show several frames taken at 10 K, and at 2 T (Fig. 3(a-d)) and 10 T (Fig. 3(e-h)). We show as red circles the positions for all vortices in all frames. All acquired maps are discussed and presented in the Supplementary Information Section IV and the Supplementary Figures 5-10. The vortex nearest neighbors are found following Delaunay triangulation and shown by the black lines in Fig. 3(a-c,e-g). We first remark that most vortices stay at roughly the same position in the different tunneling conductance maps. At 2 T (Fig. 3(a-c)), there are however several vortices which move considerable distances.

As we show in Fig. 3(d), at 2 T, these vortices travel distances far above the average intervortex distance. We have calculated the accumulated maximal distance traveled by vortices within the time frame of Fig. 3 (~ 150 minutes) at each magnetic field and temperature. The result is shown as points in Fig. 4(a). We can see that low magnetic fields allow for a strong vortex mobility by thermal fluctuations. Around 8 T and 10 T the vortex presenting largest mobility travels less than the intervortex

distance (18 nm for 8 T and 16 nm for 10 T). It is relevant to note that data for all temperatures roughly fall into a single curve.

We can now compare with macroscopic measurements (Fig. 4(b)). Maroon and grey shaded temperatures and magnetic fields represent vortex solid and liquid phases as obtained from macroscopic measurements from Refs [50, 65]. Points show the temperatures and magnetic fields which we have explored. We see that the temperature and field range where we observe vortex liquid droplets goes down to 0.5 T_c. Furthermore, we also remark that there can be a certain relationship between thermally induced vortex mobility Fig. 4(a) and the lowest temperature at which we observe liquid vortex droplets. When the vortex mobility is smallest at 8 T, the temperature for the appearance of liquid vortex droplets tends to be closer to T_c.

We note that vortex fluctuations are not always occurring at time scales smaller than our measurement time. In the Supplementary Information Section V we discuss an extreme case of slow vortex fluctuation, where a vortex is observed to jump between two different positions which evolve with time at the scale of hours. Generally, our data are taken with increasing temperature. We do not observe temperature induced hysteresis phenomena. Al-

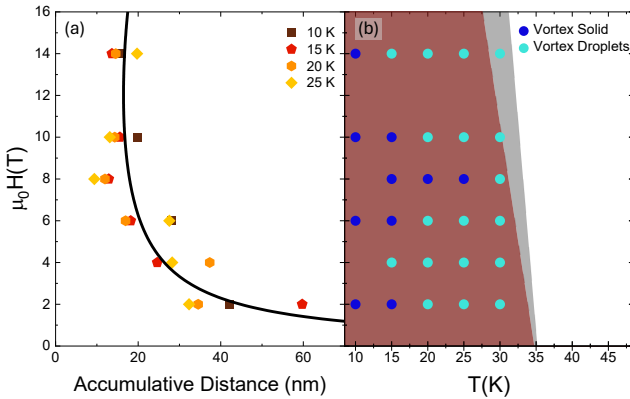


FIG. 4. Vortex melting phase diagram obtained from local measurements. In (a) we show the distance traveled by vortices through thermal motion as a function of the magnetic field, for the temperatures provided in the legend. These data are taken inside areas with a well defined vortex solid. The black line corresponds to the displacement calculated using the vortex pinning force density f_n given by the Dew-Hughes model [64] with parameters $H_{c2} = 50$ T, $p = 0.95$ and $q = 3$. In (b), we show the phase diagram from macroscopic measurements, obtained from Refs. [50, 65], with grey and maroon areas representing vortex solid and vortex liquid phases. We show as circles the temperatures and fields that we have explored. Dark blue circles signal areas where we observe a vortex solid, resolving individual vortices over nearly the whole field of view. With cyan circles, we show temperatures and fields where we have found vortex liquid droplets or areas with strongly fluctuating vortices.

though this point probably requires more measurements, out of the scope of present work, it is not very surprising given the large time scales needed for our measurements.

DISCUSSION

The vortex liquid droplets observed here occur at temperatures well below the temperature where the vortex liquid is identified from macroscopic magnetization [48, 50, 65–67], and magnetic force microscopy measurements of individual vortices at small magnetic fields (up to 0.008 T) [53]. On the other hand, transport and magnetization measurements have found ultrahigh critical current densities in single crystals of CaKFe₄As₄ [50, 57]. Uniquely to this material, critical currents have shown a non-monotonic temperature and magnetic dependence, i.e., critical currents at 20 K exceed those at 5 K at high magnetic fields ($\gtrsim 2$ T) [68, 69]. This effect is more pronounced than previously observed “fish-tail” magnetization curves in cuprates [70] and other iron-based superconductors [71–76] and suggests a distinctive vortex pinning situation. Along the same line, planar defects, CaFe₂As₂ and KFe₂As₂ intergrown layers, are the main vortex pinning centers (see also Supplementary Information Section I and Supplementary Fig. 2) [52–

59, 68, 69, 77].

By following individual vortices we obtain that the maximal distance traveled by vortices from thermal fluctuations (Fig. 4(a)) presents a curve which is nearly independent of temperature. This curve reminds us of the ones obtained using the Dew-Hughes model from Ref. [64]. Within this model, the interplay between the elastic intervortex interaction and the pinning landscape leads to a magnetic field dependence of the pinning force which falls into a single curve for all temperatures and is of the form $\propto h^p(1 - h)^q$ with $h = \frac{H}{H_{c2}}$ and p and q being two fitting parameters. Our data follow this field dependence, as shown by the black line in Fig. 4(a), using $H_{c2} = 50$ T, $p = 0.95$ and $q = 3$. Assuming that the maximal distance traveled we determine here is directly related to the pinning force, we find that the field where the force is maximal (the traveled distance minimal) is of $h_{max} \approx 0.24$, similar to the value of $h_{max} \approx 0.28$ found in Ref. [50, 78] for single crystals. The model predicts a pinning mechanism governed by surface pinning for normal center of core interaction for $h_{max} = 0.2$, and by point cores for $h_{max} = 0.33$ [64]. We expect that the CaFe₂As₂ and KFe₂As₂ intergrowth layers act as these surface-like pinning centers. The scaling of the observed traveled distance is quite good (all data points falling into a single dependence in Fig. 4(a)) but it is not perfect either. This suggests that a single mechanism does not govern the pinning; point-like disorder and pinning induced by the large linear defects (see Supplementary Information Section I) possibly coexist and have both a strong influence in vortex positions. We also find that, independently of the pinning centers, the minimum motion of the vortices corresponds directly with the place in the phase diagram (Fig. 4(b)) where the vortex solid is more resistant to the formation of local vortex liquid droplets. This illustrates how the pinning potential landscape governs the motion of vortices and the formation of vortex liquid droplets alike.

We note that the vortex lattice in a material with a strong four-fold anisotropy in the normal density of states, as CaKFe₄As₄, might show at sufficiently high magnetic fields a transition between hexagonal and square ordered vortex lattices [79–81]. It seems that vortices are too disordered in present samples of CaKFe₄As₄ to establish such a phase transition over macroscopic length scales [51]. However, elastic moduli are strongly influenced by electronic interactions and some moduli, as the rotation modulus, can vanish at certain conditions [82]. This feature could favor the formation of places with strong vortex fluctuations.

Our data raise the question about the observation of a finite voltage in macroscopic critical current measurements. Possibly, even in presence of large amounts of vortex liquid droplets, sufficiently large samples still present zero voltage drop, owing to the formation of percolation paths for current flow [83]. Nevertheless, small micron sized samples, as those used in research of two-dimensional materials and in nanostructured supercon-

ductors, should be much more sensitive to the formation of vortex liquid droplets [84–87].

We note that up-to-date measurements of the melting transition in two-dimensional vortex solids, obtained in thin films with a perpendicular magnetic field, present a melting transition where fluctuations induce defects in an otherwise ordered hexagonal lattice [28–30, 33–35]. The transition to a vortex liquid where individual vortices are no longer resolved with STM occurs over large portions of the sample. The observation of vortex liquid droplets here shows a distinct pinning landscape consisting of a combination of crystal lattice and defects in $\text{CaKFe}_4\text{As}_4$.

CONCLUSION

In summary, we have imaged superconducting vortices as a function of temperature and magnetic field in the iron based superconductor $\text{CaKAs}_4\text{Fe}_4$. We have observed a disordered vortex solid at low temperatures which melts locally, forming vortex liquid droplets well below the vortex melting temperature. Thus, the melting of vortices in superconductors is not a uniform transition, but is strongly linked to the local pinning potential. We have explored this link directly, by characterizing thermally activated vortex motion and finding a close relationship between vortex pinning and thermally induced motion. Our data reveal a broad crossover region where solid, and liquid vortex phases coexist. This suggests that the actual dissipationless superconducting phase has a much smaller temperature range than what can be found from macroscopic experiments, underscoring the fundamental relevance of studies aimed to enhance vortex pinning for building functional superconducting devices.

ACKNOWLEDGEMENTS

This work was supported by the Spanish Research State Agency (TED2021-130546BI00, PID2023-1501480B-I00 and CEX2023001316-M), Comunidad de Madrid through project TEC-2024/TEC-380 “Mag4TIC”, the EU through grant agreement No 871106 and by the European Research Council PNICTEYES grant agreement 679080 and VECTORFIELDIMAGING grant agreement 101069239. We acknowledge the QUASURF project (SI4/PJI/2024-00199) funded by the Comunidad de Madrid through the agreement to promote and encourage research and technology transfer at the Universidad Autónoma de Madrid. We acknowledge collaborations through EU program Cost CA21144 (www.superqumap.eu). Work at Ames National Laboratory (crystal growth, basic characterization, drafting and editing) was supported by the U.S. Department of Energy, Office of Basic Energy Science, Division of Materials Sciences and Engineering. Ames National Laboratory is operated for the U.S. Department of Energy by Iowa State University under Contract No.

DE-AC02-07CH11358. We also acknowledge SEGAIN-VEX for support in design and for construction of the temperature stabilized STM.

METHODS

Single crystals of $\text{CaKAs}_4\text{Fe}_4$ were grown and characterized following the methods described in [48, 88]. We cleaved the samples by glueing a post to the top of each sample and pushing it with the slider described in Ref. [89]. With this method, we obtained large ($> 2\mu\text{m} \times 2\mu\text{m}$), clean and atomically flat surfaces. The tip was made of gold and was conditioned (cleaning and sharpening) using a gold sample and following the methods described in Ref. [90]. We used a modified lab-built STM system, similar to the one described in Ref. [89]. The control software is described in Ref. [91] and available in Ref. [92]. Image rendering was performed mostly using the lab-built software described in Ref. [91], using occasionally imaging software as Ref. [93]. The system was introduced in a helium bath cryostat at 4.2 K on a support that was thermally anchored to a cold plate, itself thermally anchored to the helium bath [94]. We used a heater and a temperature controller to modify the temperature of the STM system. We reduced thermal creep from temperature gradients by placing the heater between the cold source and the STM holder. We maintained temperature stability of $\pm 100\text{ mK}$ up to temperatures above 40 K. We tested thermal stability by making subsequent topographic STM maps and verifying that the field of view remained the same. When required, we modified the field of view using references in the topography. To map vortices, we acquire the tunneling conductance as a function of the bias voltage. Maps are generally made by normalizing the tunneling conductance to a value at a bias voltage well above the superconducting gap (above 10 mV) and plotting as a function of the position the zero bias tunneling conductance. As the temperature variation of the tunneling conductance is quite pronounced, we maximize the color scale at each temperature (unless otherwise stated) to best visualize vortices. The superconducting state is represented as blue, and the normal state inside the vortex as yellow in the maps shown below. At each applied magnetic field we have increased the temperature in steps of 5 K between 10 K and 30 K. We also acquired several maps, one after the other at each temperature, to follow the positions of individual vortices. Each map was taken within 30 minutes. Delaunay triangulation of the vortex positions was performed using the software available in Ref. [92] and described in Refs. [29, 95–97]. Using the in-situ positioning method described in Ref. [89], we explored many different fields of view, in regions with different numbers of defects in two different samples.

DATA AVAILABILITY

The data shown in this study is available from the corresponding author upon reasonable request.

CODE AVAILABILITY

The code used to analyse this results can be found in [92].

AUTHOR CONTRIBUTIONS

OBM and JAM performed the experiments, with the supervision of EH, IG and HS. The analysis of the data and the coding of the tools used to do so were made by OBM and PGT. Samples were synthesized and characterized by MX, JS, SLB and PCC. The paper was written by OBM, JAM, IG, EH, and HS with input and approval from all authors.

COMPETING INTERESTS

The authors declare no competing interests.

CORRESPONDING AUTHOR

Corresponding author: hermann.suderow@uam.es.

SUPPLEMENTARY INFORMATION

I. SURFACE CHARACTERIZATION AND DEFECTS

In Supplementary Figure 1 we characterize the surface and its defects in three representative fields of view. The color scale following height variations along the surface in the STM topography Supplementary Figure 1(a-c) has been maximized and is of the order of the atomic scale, below 0.4 nm. This is characteristic of exposed Ca or K layers [51, 98]. In Supplementary Figure 1 (d-f), we also show height profiles, marked by a green arrow in Supplementary Figure 1 (a-c), along several linear defects on topographies shown in Supplementary Figure 1(a-c) by red dashed lines. Such linear features are often observed in CaKAs₄Fe₄ and related iron pnictide superconductors [16, 51, 99–101]. The height changes along the linear features are below an atomic size step [102] and they also present sizeable pair-breaking [51]. We can associate these linear defects with intercalated layers of CaFe₂As₂ and KFe₂As₂ [52, 68, 69, 77, 103]. Some of these layers have been found to be single atomic layers (along c-axis) and tens of nm wide (in the ab-plane) [68, 69]. Large strain fields [104] have been observed around these single intergrown layers along the c axis (perpendicular to the layer plane) [52, 77]. We expect that the corrugation observed at the surface stemming from an underlying intergrown layer is below interatomic distances, and we thus associate the linear features we observe at the surface with intergrown layers. We can find a relation between the position of these linear defects in the topography and the corresponding arrangement of vortices, as shown by the red dashed lines in the topographies (Supplementary Figure 1(a-c)) and the zero bias tunneling conductance maps (Supplementary Figure 1(g-i)). Vortices are often pinned along the linear features, as shown for example in the bottom right of Supplementary Figure 1(g). The maps show blurred vortices along these lines. This suggests that vortices are strongly fluctuating along the linear features. Moreover, we observe that vortex positions (Supplementary Figure 1(g-i)) are oriented following these linear features. In Supplementary Figure 2 we schematically present a possible arrangement of vortex positions and intergrowth of CaFe₂As₂ and KFe₂As₂.

II. VORTEX CORE SIZE VS TEMPERATURE

In Supplementary Figure 3 we show the dependence of the vortex core size as a function of the magnetic field and temperature. We observe that at low temperatures the vortex core size roughly follows the zero temperature magnetic field dependence [105]. However, at high temperatures (yellow triangles in Supplementary Figure 3), vortex jitter leads to an effective increase in the vortex core size at large magnetic fields.

III. MELTING

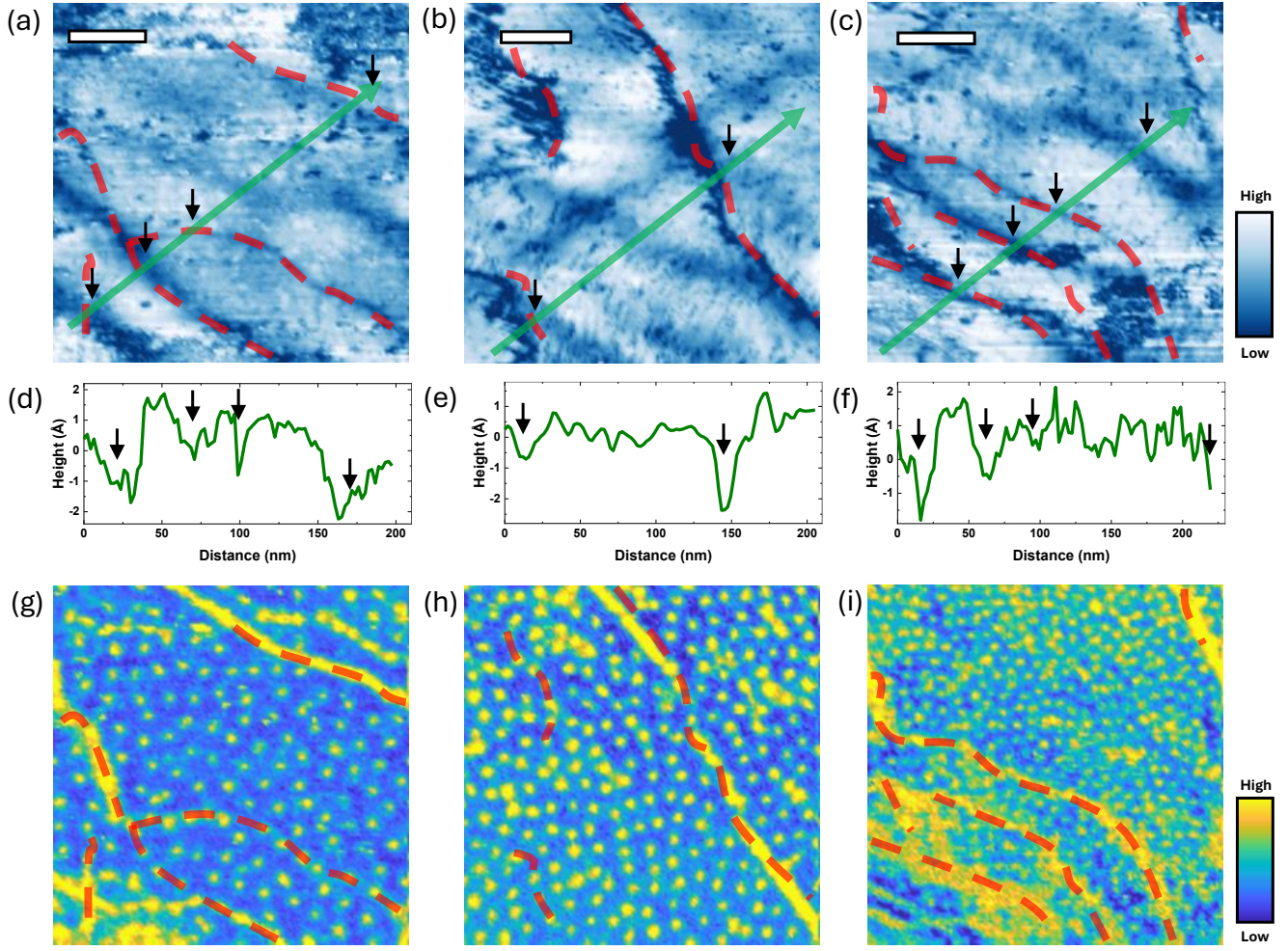
In Supplementary Figure 4 we show examples of zero bias conductance maps at several temperatures (columns) and magnetic fields (rows). At the lowest temperatures we observe a disordered vortex solid in all cases. We also observe areas, marked by the red lines, where individual vortices are no longer resolved over a distance exceeding several times the intervortex distance. Within the same field of view, we also observe areas with a vortex solid. At 8 T the vortex solid is observed until very close to T_c . Just below T_c we observe a vortex liquid in the full field of view. The melting temperature is at this magnetic field very close to the one obtained from macroscopic experiments.

IV. VORTEX TRAJECTORIES

In Supplementary Figures 5–10 we show a few tunneling conductance maps from a series of maps taken sequentially in the same field of view, for the temperatures marked in each figure and for magnetic fields ranging from 2 T (Supplementary Figure 5) to 14 T (Supplementary Figure 10). We show half of all measured maps taken in each case. In every figure, we show in the right column the vortex positions for all frames as red dots. The red lines show the changes in the vortex positions in subsequent images. We ensured continuity by requiring displacements between successive images to remain well below the intervortex spacing. We highlight in white the vortex that presented the largest motion. We obtained the accumulative distance from the sum of the displacements of each vortex. We plot in Figure 4(a) of the main text the accumulated distance of the vortex showing largest motion (in white in the right column of Figs. 5–10). For low and high magnetic fields (2 T Supplementary Figure 5, 4 T Supplementary Figure 6 and 14 T Supplementary Figure 10) there are several vortices which move across large distances as compared to the intervortex separation. By contrast, for intermediate fields such as in 8 T Supplementary Figure 8 and 10 T Supplementary Figure 9 most of the vortices remain at the same position. There is no strong temperature dependence of the maximal vortex motion, in agreement with the values of the maximal accumulated distance falling onto each other for each magnetic field in Figure 4(a) of the main text.

V. SEPARATION OF VORTICES

Changes in the vortex positions due to thermal fluctuations (Figure 1(b) of the main text) lead to an increase in the zero bias conductance around the vortex core with respect to the absence of fluctuations (Figure 1(a) of the main text). The time scale involved in the fluctuations depends on the temperature and the pinning landscape



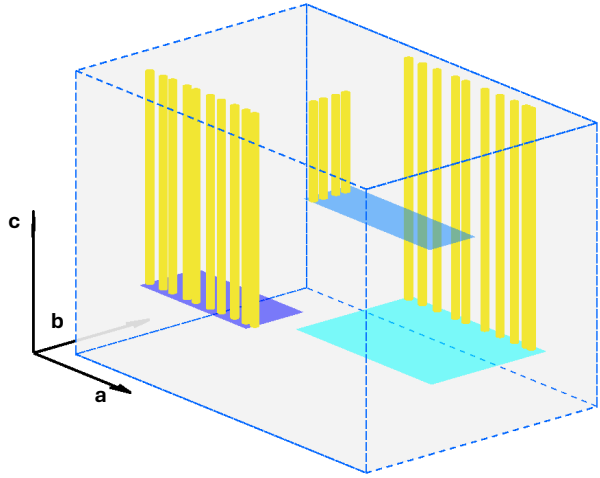
Supplementary Figure 1. **Comparison of topography and zero bias conductance maps.** (a,b,c) STM topography corresponding to the zero bias tunneling conductance map acquired simultaneously and shown in (g-i). White bars correspond to 40 nm. The color scale corresponds to height changes of about 0.4 nm. (d-f) Height profile as a function of position along the line scan shown as a green arrow in (a-c), respectively. Red dashed lines mark the largest defects identified from the STM topography. We mark the position of linear defects with black arrows in both topography and height profiles. (g-i) The zero bias tunneling conductance map acquired simultaneously as topographies in (a-c). The color scale corresponds to conductance changes of about 0.8 times the tunneling conductance normalized to its normal state value (i.e. in many yellow areas, the superconducting gap is very weak but remains generally open). Red dashed lines mark the largest defects identified in the STM topography. Maps taken at 10 K and 6 T for a,g; at 10 K and 10 T for b,h; and at 15 K and 14 T for c,i.

and mostly involves rapid fluctuations, as schematically shown in Figure 1 of the main text. However, when vortices are in between close-lying pinning centers, fluctuations might considerably slow [107, 108]. We discuss an extreme example of this phenomenon now.

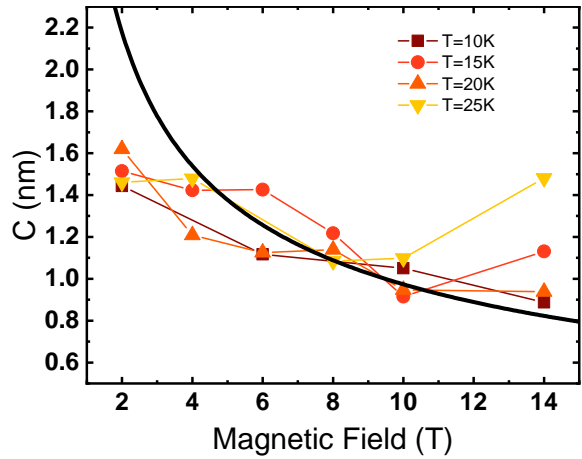
In Supplementary Figure 11 we present a zoom to a certain area at 10 T and 10 K. We mark in Supplementary Figure 11(a-b) (left panels) one vortex by a dashed circle. Apparently, this is a single vortex. However, tracing the conductance profile as a function of the position through the apparent vortex center leads to a two-peak structure (right panels in Supplementary Figure 11). We can fit the profile using two Gaussians located approximately 10 nm apart. The average intervortex distance at 10 T is

of about 15 nm and the vortex core size, see Section II, is below 2 nm. This suggests that the feature observed in the zero bias tunneling conductance marked by the white dashed circle in Supplementary Figure 11 is composed of two vortices. Indeed, with time, this feature separates into two features, as shown by the white dashed ellipses in the left panels of Figs. 11(c-f). The vortex profiles (shown in the right panels of Figs. 11(c-f)) consist now of two well-separated Gaussian shapes. Their separation reaches the intervortex distance for this magnetic field at the end of the sequence (Supplementary Figure 11(f)).

This slowly fluctuating vortex is an extreme example of vortex fluctuations on long time scales and occurs in an area where the rest of the vortices are well pinned.

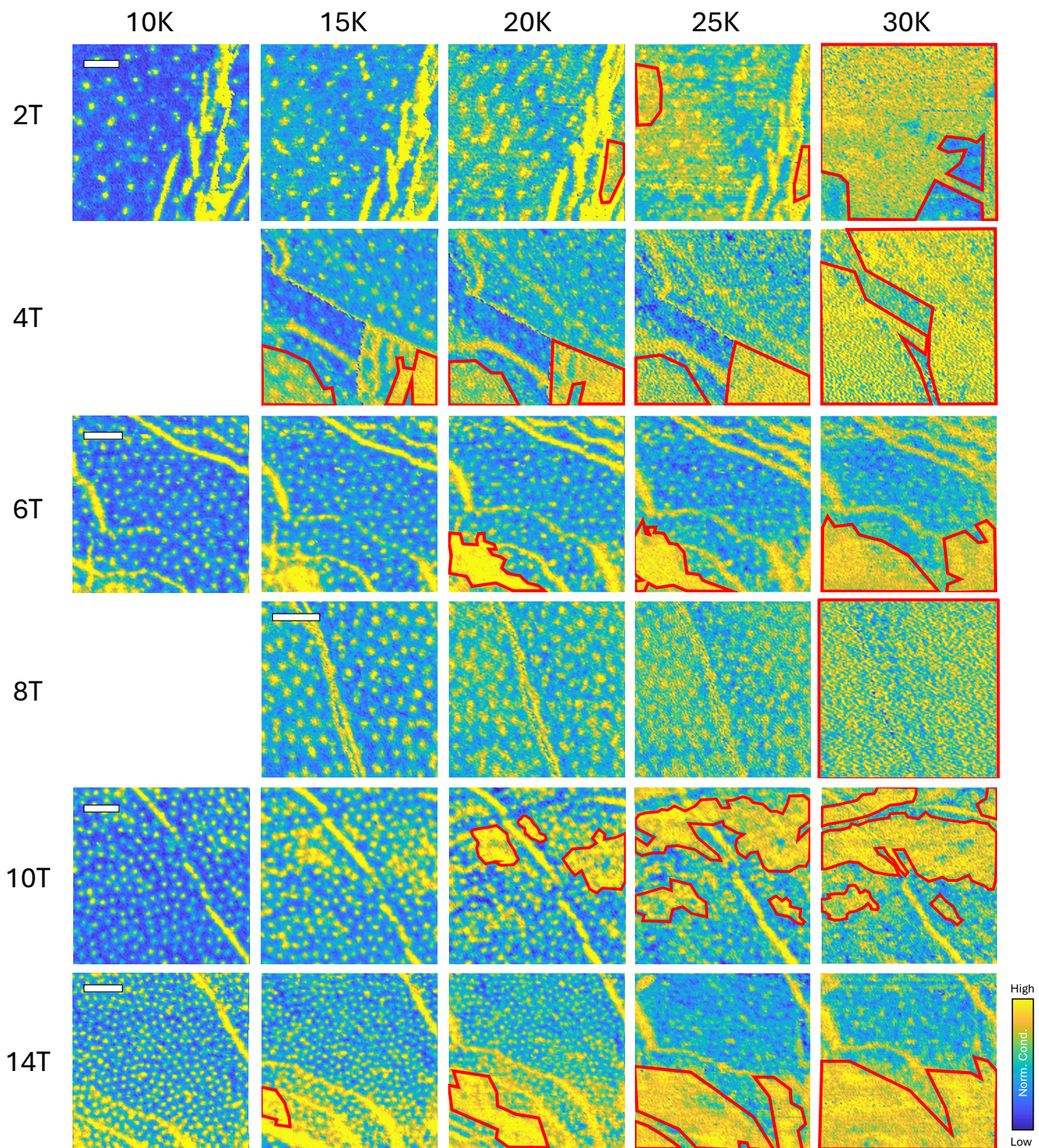


Supplementary Figure 2. **Possible role of defects and intergrowth in vortex pinning of $\text{CaKAs}_4\text{Fe}_4$.** Schematic representation of the $\text{CaKFe}_4\text{As}_4$ crystal lattice with an interstitial single layers of CaFe_2As_2 or KFe_2As_2 marked with an blue planes. We represent the vortices as yellow cylinders that become pinned on the borders of these interstitial layers.

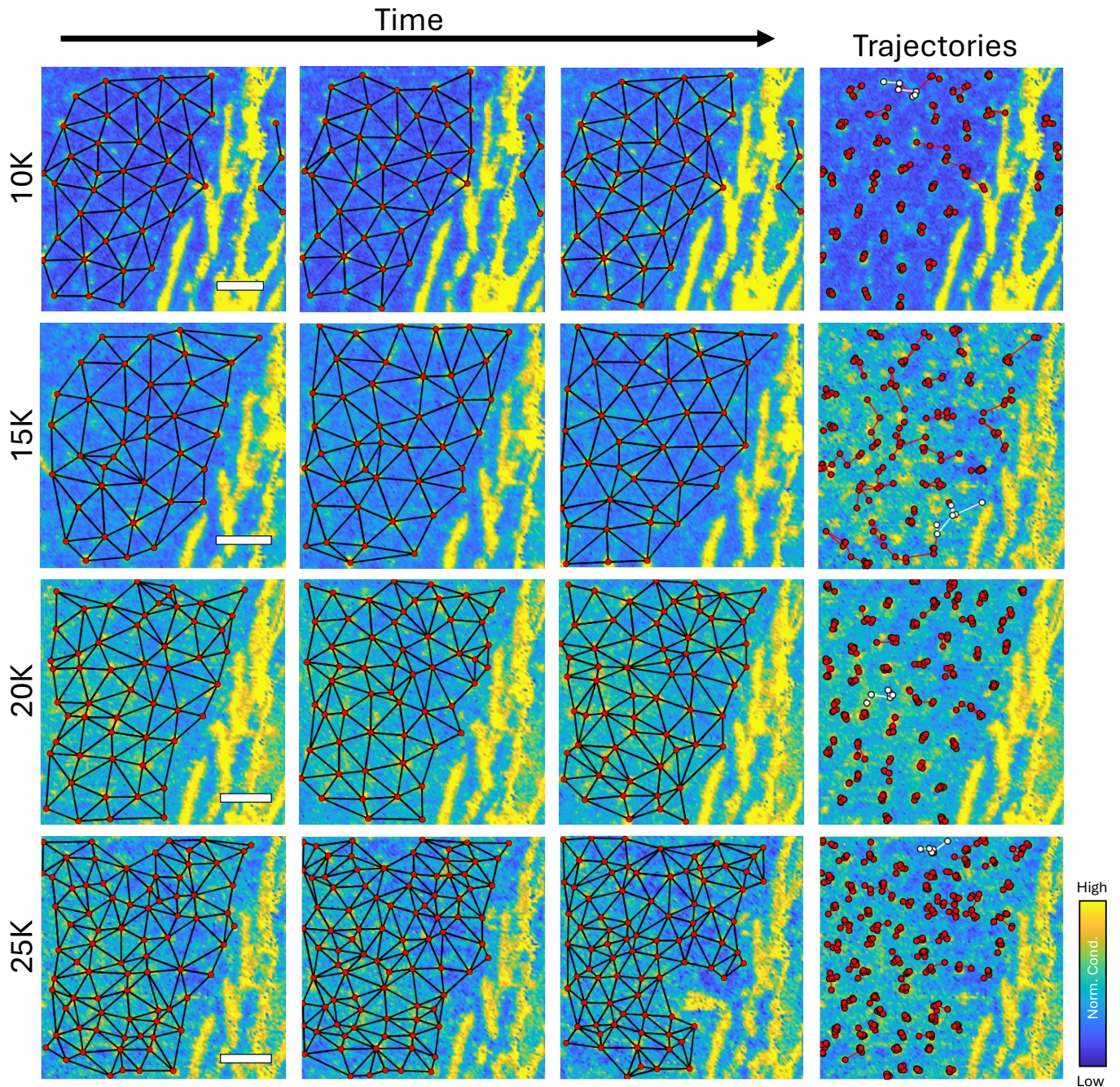


Supplementary Figure 3. **Vortex core size, C as a function of magnetic field.** The continuous black line is given by $C \propto 1/\sqrt{H}$, and is the behavior expected for the zero temperature extrapolation and found at low temperatures in $\text{CaKFe}_4\text{As}_4$ [105, 106].

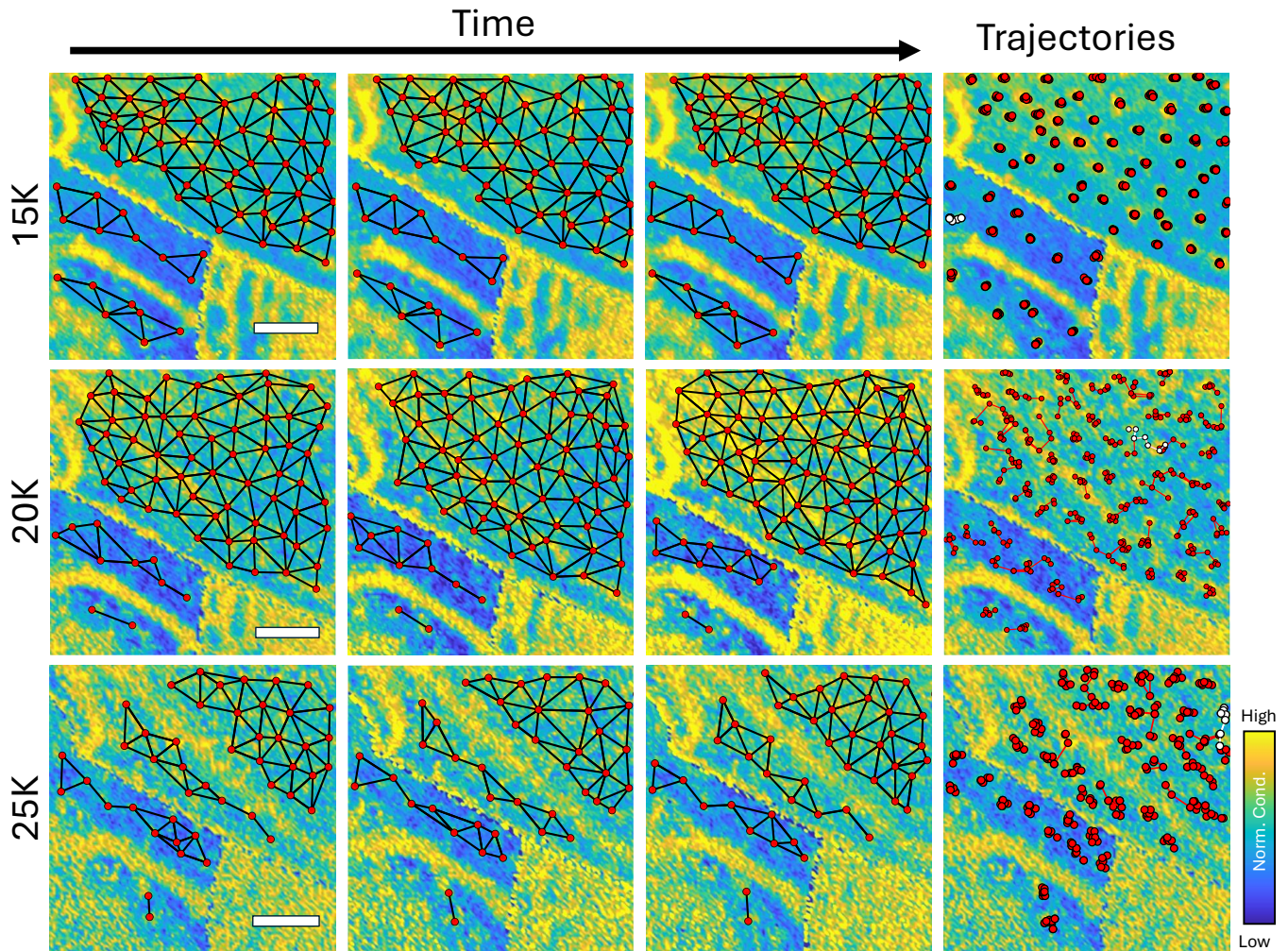
The areas where we observe vortex droplets (red areas in Figure 2 (c-e) of the main text) generally coincide with areas where subsequently acquired tunneling conductance maps present vortices fluctuating slightly around a certain position, for example at the top left and right parts of the tunneling conductance map of Figure 2(b) of the main text.



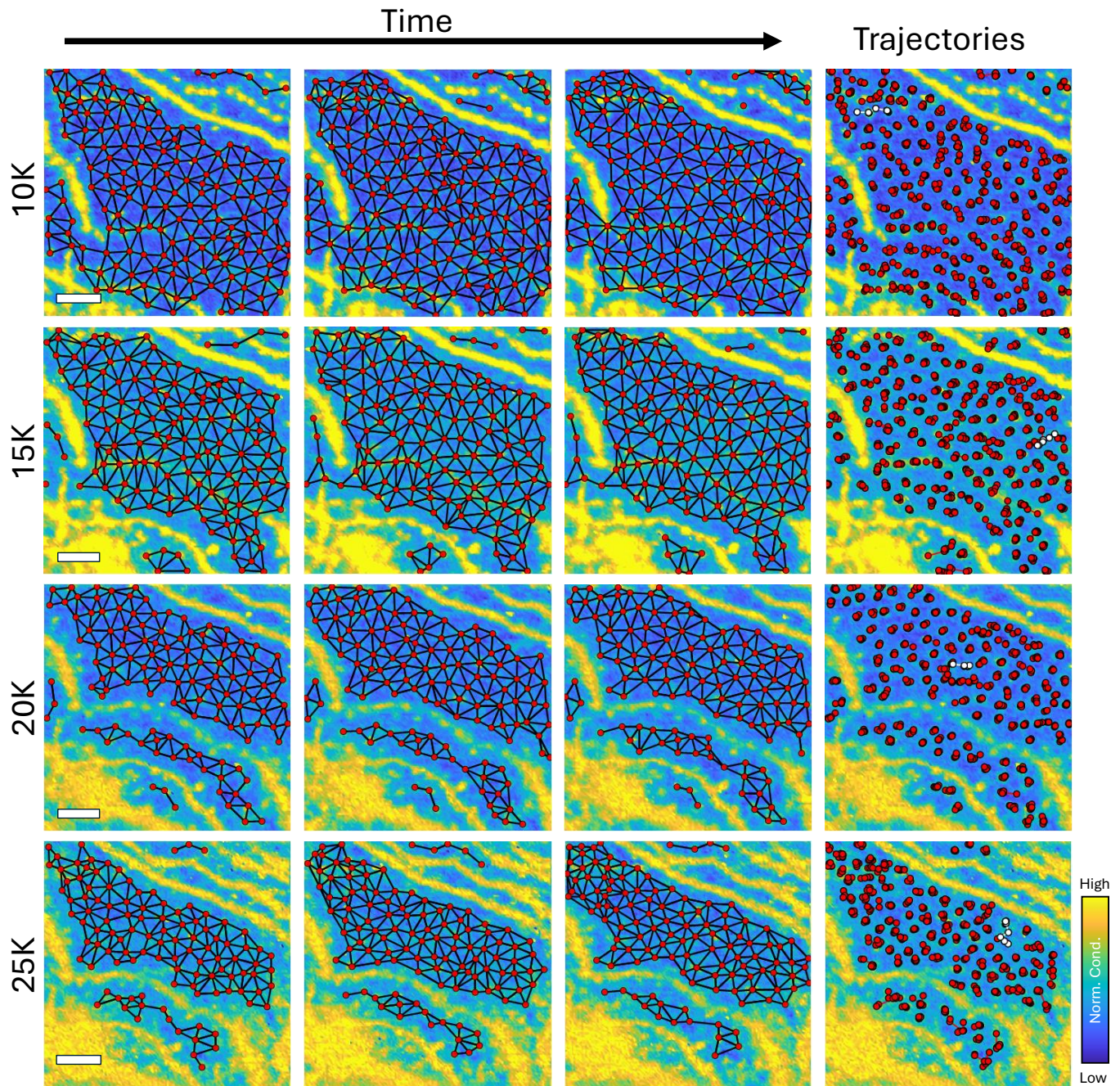
Supplementary Figure 4. **Zero bias tunneling conductance maps as a function of the magnetic field and temperature.** Areas with vortex liquid are marked by red lines. White bars correspond to 40 nm.



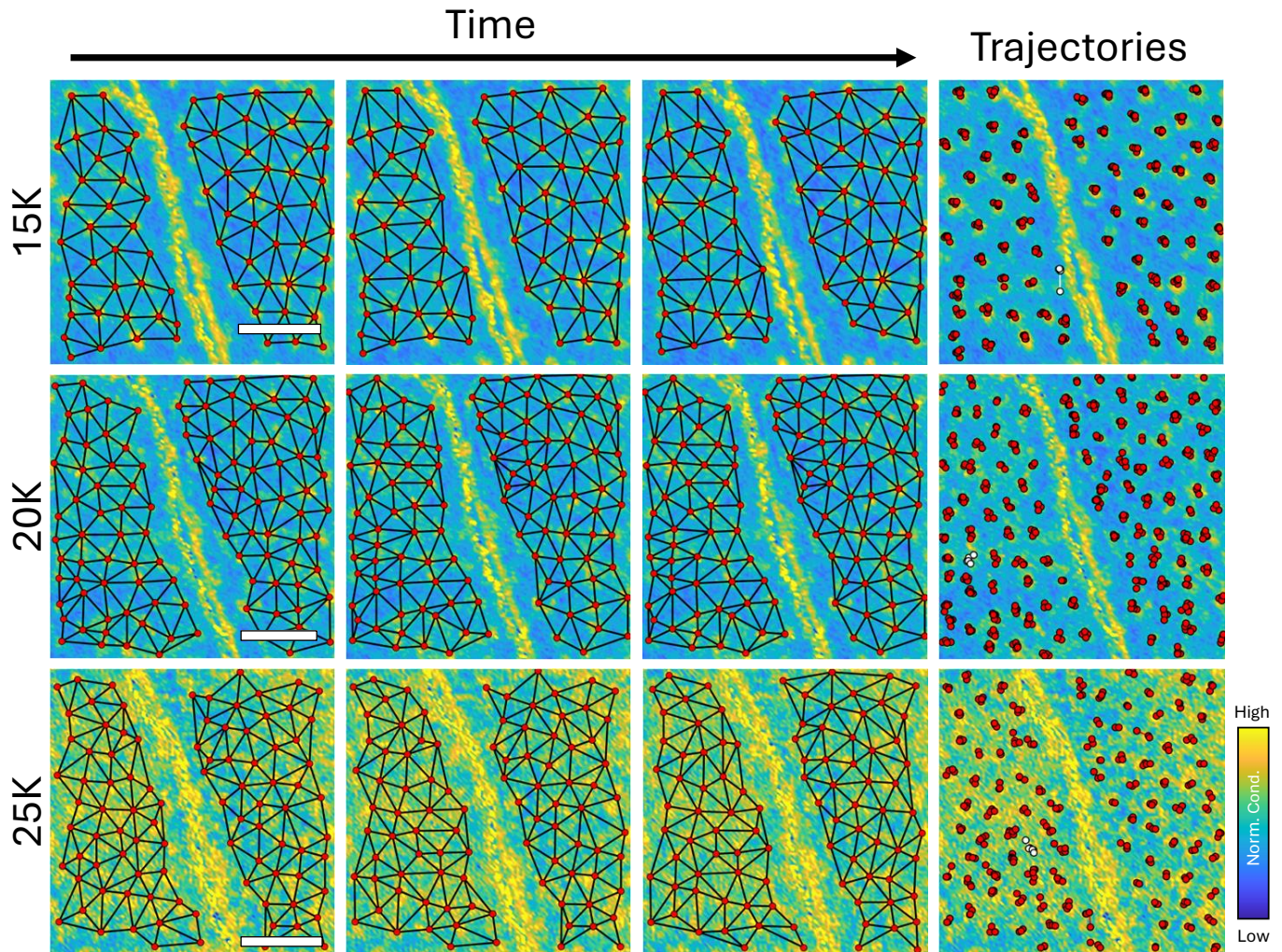
Supplementary Figure 5. **Zero bias tunneling conductance maps at 2 T.** Each row corresponds to images taken at different temperatures (10 K-25 K) in the same field of view. The first three columns show three representative images at the start (left), middle (middle) and end (right) of the sequence. The red dots mark the positions of the vortices, and the black lines connecting them are the triangulation of the vortex positions. The last column shows the extracted trajectories, with red lines joining the vortex positions in different frames. The vortex highlighted in white is the one that shows the largest accumulated distance. White bars correspond to 40 nm.



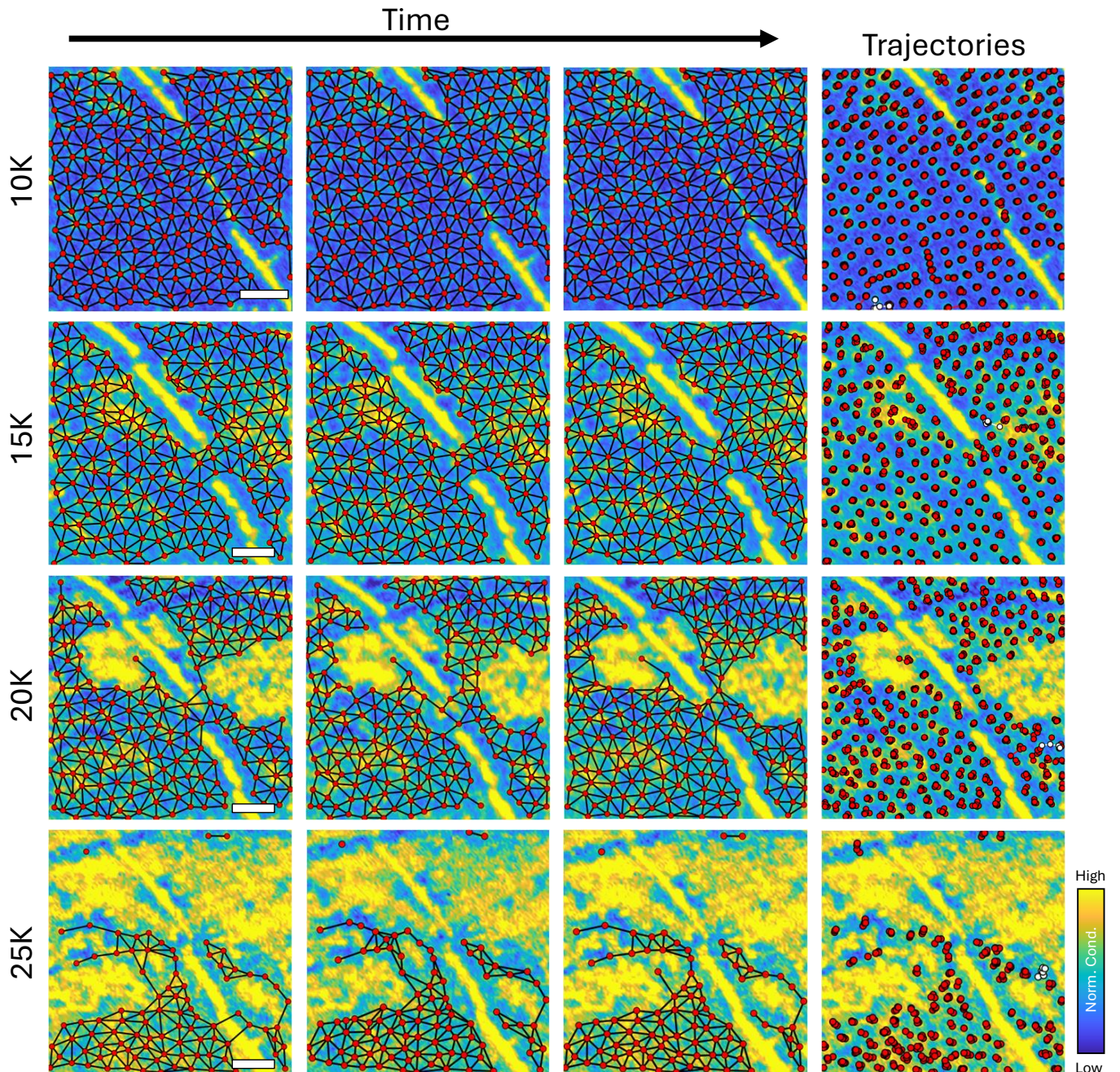
Supplementary Figure 6. **Zero bias tunneling conductance maps at 4 T.** Each row corresponds to images taken at different temperatures (15 K-25 K) in the same field of view. The first three columns show three representative images at the start (left), middle (middle) and end (right) of the sequence. The red dots mark the positions of the vortices, and the black lines connecting them are the triangulation of the vortex positions. The last column shows the extracted trajectories, with red lines joining the vortex positions in different frames. The vortex highlighted in white is the one that shows the largest accumulated distance. White bars correspond to 40 nm.



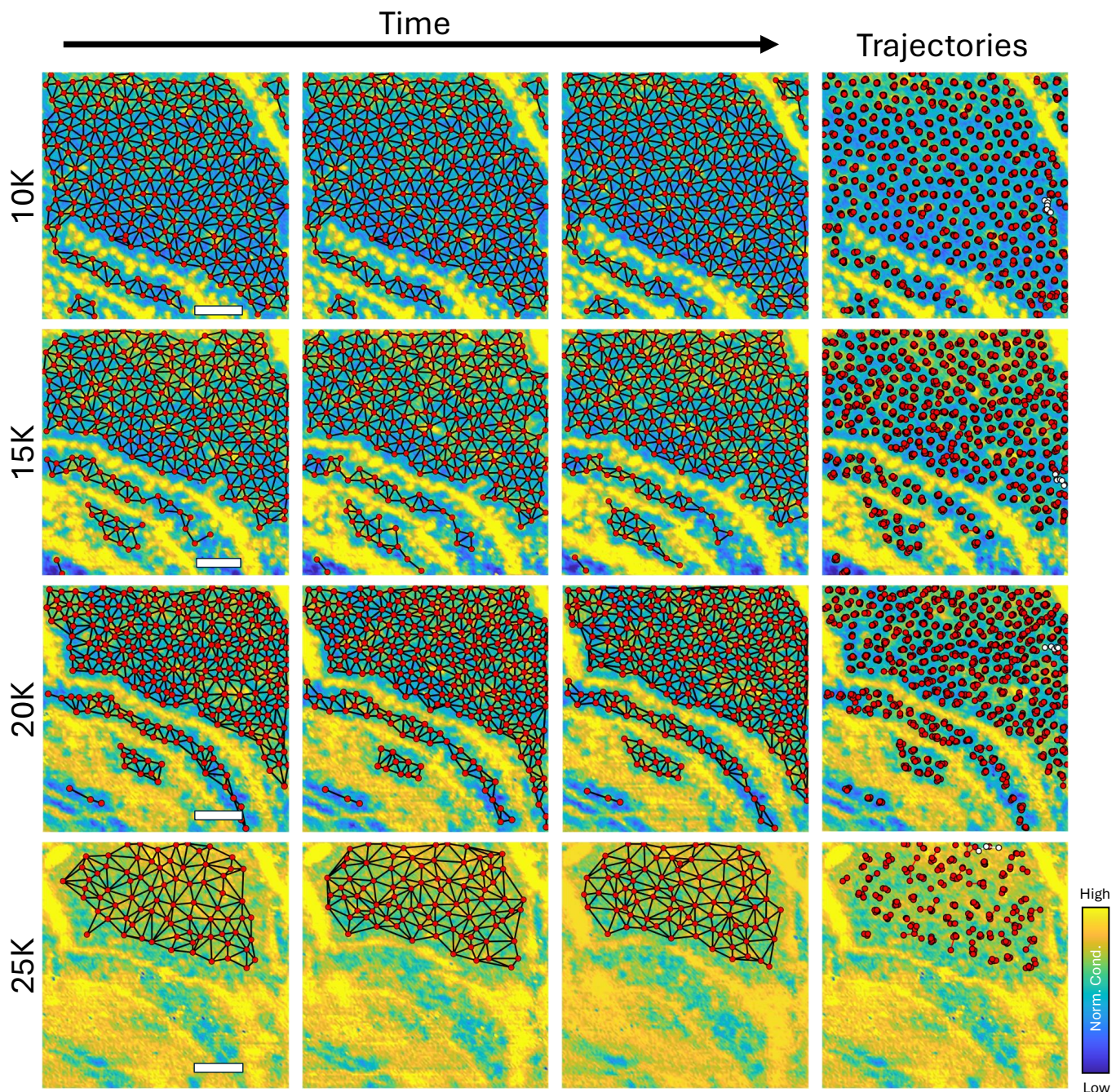
Supplementary Figure 7. **Zero bias tunneling conductance maps at 6 T.** Each row corresponds to images taken at different temperatures (10 K-25 K) in the same field of view. The first three columns show three representative images at the start (left), middle (middle) and end (right) of the sequence. The red dots mark the positions of the vortices, and the black lines connecting them are the triangulation of the vortex positions. The last column shows the extracted trajectories, with red lines joining the vortex positions in different frames. The vortex highlighted in white is the one that shows the largest accumulated distance. White bars correspond to 40 nm.



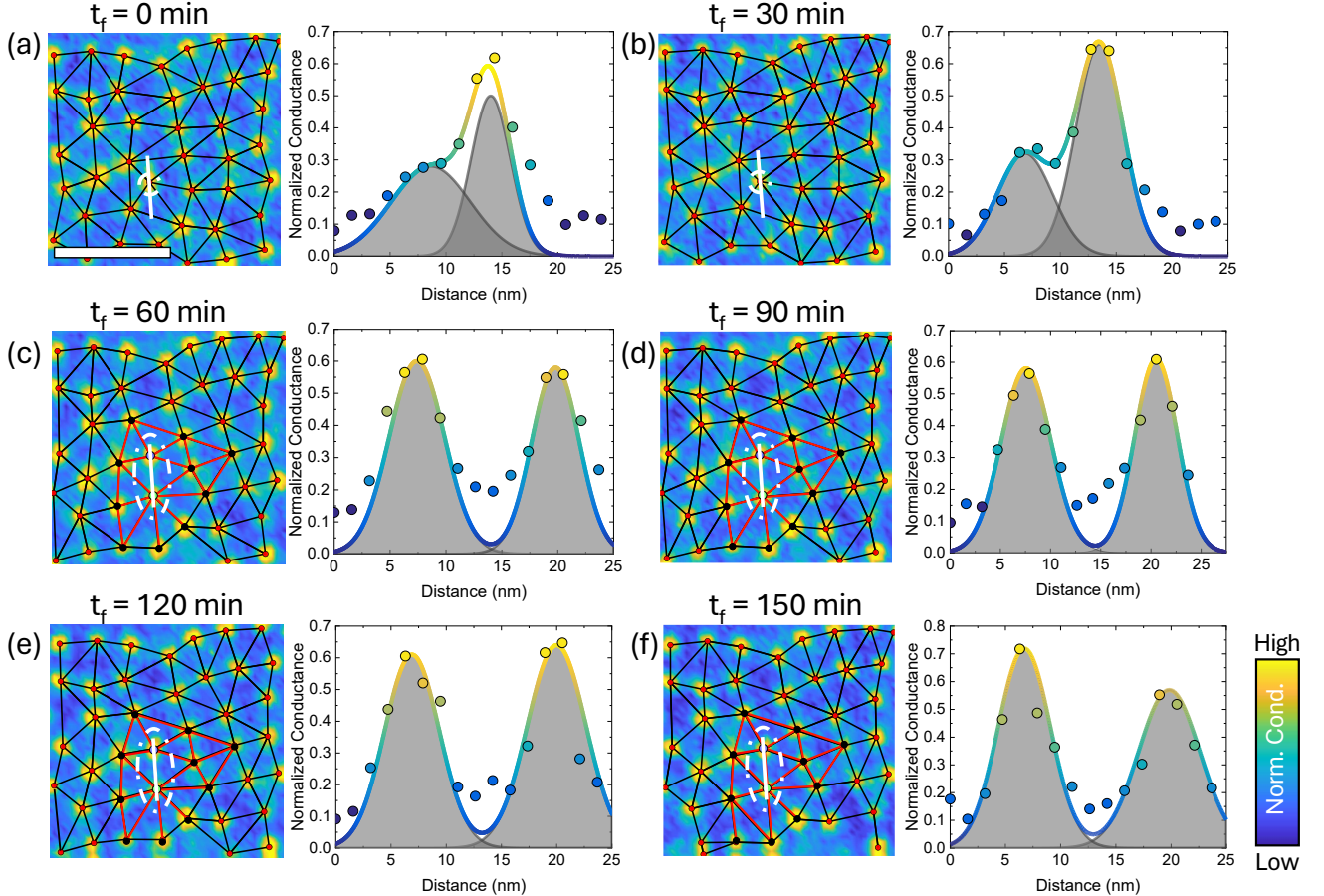
Supplementary Figure 8. Zero bias tunneling conductance maps at 8 T. Each row corresponds to images taken at different temperatures (15 K-25 K) in the same field of view. The first three columns show three representative images at the start (left), middle (middle) and end (right) of the sequence. The red dots mark the positions of the vortices, and the black lines connecting them are the triangulation of the vortex positions. The last column shows the extracted trajectories, with red lines joining the vortex positions in different frames. The vortex highlighted in white is the one that shows the largest accumulated distance. White bars correspond to 40 nm.



Supplementary Figure 9. **Zero bias tunneling conductance maps at 10 T.** Each row corresponds to images taken at different temperatures (10 K-25 K) in the same field of view. The first three columns show three representative images at the start (left), middle (middle) and end (right) of the sequence. The red dots mark the positions of the vortices, and the black lines connecting them are the triangulation of the vortex positions. The last column shows the extracted trajectories, with red lines joining the vortex positions in different frames. The vortex highlighted in white is the one that shows the largest accumulated distance. White bars correspond to 40 nm.



Supplementary Figure 10. **Zero bias tunneling conductance maps at 14 T.** Each row corresponds to images taken at different temperatures (10K-25 K) in the same field of view. The first three columns show three representative images at the start (left), middle (middle) and end (right) of the sequence. The red dots mark the positions of the vortices, and the black lines connecting them are the triangulation of the vortex positions. The last column shows the extracted trajectories, with red lines joining the vortex positions in different frames. The vortex highlighted in white is the one that shows the largest accumulated distance. White bars correspond to 40 nm.



Supplementary Figure 11. **Vortex fluctuations in a small field of view.** In panels (a–f) we focus on the portion of the 10 T maps showing an extreme example of slow vortex creep, presenting subsequently acquired maps from (a) to (f). We show again the zero bias tunneling conductance maps, together with vortex positions (red circles) and nearest neighbor structure (black lines) in the left panels. Red lines connecting the red circles correspond to the lines of the triangulation modified by the splitting of an apparent single vortex in (c). In the right panels, we show profiles of the tunneling conductance as dots and fits to Gaussians as lines. Each Gaussian is shown separately in grey below the fit. We mark with a white dashed circle in the left panels an area which seems to contain a single vortex in (a), which splits into two after 150 minutes in (f). White bar in (a) correspond to 40 nm.

[1] Abrikosov, A. On the magnetic properties of superconductors of the second group. *Sov. Phys. J. Exp. Theor. Phys.* **32**, 1442 (1957). <https://cir.nii.ac.jp/crid/1370572092770837894>.

[2] Blatter, G., Feigel'man, M. V., Geshkenbein, V. B., Larkin, A. I. & Vinokur, V. M. Vortices in high-temperature superconductors. *Reviews of modern physics* **66**, 1125 (1994). <https://link.aps.org/doi/10.1103/RevModPhys.66.1125>.

[3] Brandt, E. H. The flux-line lattice in superconductors. *Reports on Progress in Physics* **58**, 1465 (1995). <https://iopscience.iop.org/article/10.1088/0034-4885/58/11/003>.

[4] Nelson, D. R. & Vinokur, V. Boson localization and correlated pinning of superconducting vortex arrays. *Physical Review B* **48**, 13060 (1993). <https://link.aps.org/doi/10.1103/PhysRevB.48.13060>.

[5] Klein, T. *et al.* A Bragg glass phase in the vortex lattice of a type II superconductor. *Nature* **413**, 404–406 (2001). <https://doi.org/10.1038/35096534>.

[6] Mikitik, G. P. & Brandt, E. H. Effect of pinning on the vortex-lattice melting line in type-II superconductors. *Phys. Rev. B* **68**, 054509 (2003). <https://link.aps.org/doi/10.1103/PhysRevB.68.054509>.

[7] Kierfeld, J. & Vinokur, V. Lindemann criterion and vortex lattice phase transitions in type-II superconductors. *Phys. Rev. B* **69**, 024501 (2004). <https://link.aps.org/doi/10.1103/PhysRevB.69.024501>.

[8] Dew-Hughes, D. The critical current of superconductors: an historical review. *Low Temperature Physics* **27**, 713–722 (2001). <https://doi.org/10.1063/1.1401180>.

[9] Campbell, A. & Evetts, J. Flux vortices and transport currents in type II superconductors. *Advances in Physics* **21**, 199–428 (1972). <https://doi.org/10.1080/00018737200101288>.

[10] Hyun, O. B., Finnemore, D. K., Schwartzkopf, L. & Clem, J. R. Elementary pinning force for a superconducting vortex. *Phys. Rev. Lett.* **58**, 599–601 (1987). <https://link.aps.org/doi/10.1103/PhysRevLett.58.599>.

[11] Breitwisch, M. & Finnemore, D. K. Pinning of a single abrikosov vortex in superconducting Nb thin films using artificially induced pinning sites. *Phys. Rev. B* **62**, 671–677 (2000). <https://link.aps.org/doi/10.1103/PhysRevB.62.671>.

[12] Ginzburg, V. Some remarks on phase transitions of the second kind and the microscopic theory of ferroelectric materials. *Soviet Phys. Solid State* **2**, 1824–1834 (1961). <https://cir.nii.ac.jp/crid/157226154973336704>.

[13] Levanyuk, A. Contribution to the theory of light scattering near the second-order phase-transition points. *Sov. Phys. JETP* **9**, 571–576 (1959).

[14] Eley, S., Miura, M., Maiorov, B. & Civale, L. Universal lower limit on vortex creep in superconductors. *Nature Materials* **16**, 409–413 (2017). <https://doi.org/10.1038/nmat4840>.

[15] Mikitik, G. P. & Brandt, E. H. Peak effect, vortex-lattice melting line, and order-disorder transition in conventional and high- T_c superconductors. *Phys. Rev. B* **64**, 184514 (2001). <https://link.aps.org/doi/10.1103/PhysRevB.64.184514>.

[16] Koshelev, A. *et al.* Melting of vortex lattice in the magnetic superconductor RbEuFe₄As₄. *Physical Review B* **100**, 094518 (2019). <https://link.aps.org/doi/10.1103/PhysRevB.100.094518>.

[17] Zeldov, E. *et al.* Thermodynamic observation of first-order vortex-lattice melting transition in Bi₂Sr₂CaCu₂O₈. *Nature* **375**, 373–376 (1995). <https://doi.org/10.1038/375373a0>.

[18] Safar, H. *et al.* Experimental evidence for a first-order vortex-lattice-melting transition in untwinned, single crystal YBa₂Cu₃O₇. *Physical review letters* **69**, 824 (1992). <https://link.aps.org/doi/10.1103/PhysRevLett.69.824>.

[19] Willemin, M. *et al.* First-order vortex-lattice melting transition in YBa₂Cu₃O_{7- δ} near the critical temperature detected by magnetic torque. *Physical review letters* **81**, 4236 (1998). <https://link.aps.org/doi/10.1103/PhysRevLett.81.4236>.

[20] Paltiel, Y. *et al.* Dynamic instabilities and memory effects in vortex matter. *Nature* **403**, 398–401 (2000). <https://doi.org/10.1038/35000145>.

[21] Schilling, A. *et al.* Anisotropic latent heat of vortex-lattice melting in untwinned YBa₂Cu₃O_{7- δ} . *Phys. Rev. Lett.* **78**, 4833–4836 (1997). <https://link.aps.org/doi/10.1103/PhysRevLett.78.4833>.

[22] Cubitt, R. *et al.* Direct observation of magnetic flux lattice melting and decomposition in the high- T_c superconductor Bi_{2.15}Sr_{1.95}CaCu₂O_{8+ δ} . *Nature* **365**, 407–411 (1993). <https://doi.org/10.1038/365407a0>.

[23] Avraham, N. *et al.* 'Inverse' melting of a vortex lattice. *Nature* **411**, 451–454 (2001). <https://doi.org/10.1038/35078021>.

[24] Yaron, U. *et al.* Structural evidence for a two-step process in the depinning of the superconducting flux-line lattice. *Nature* **376**, 753–755 (1995). <https://doi.org/10.1038/376753a0>.

[25] Hess, H. F., Robinson, R. B., Dynes, R. C., Valles, J. M. & Waszcza, J. V. Scanning-tunneling-microscope observation of the Abrikosov flux lattice and the density of states near and inside a fluxoid. *Phys. Rev. Lett.* **62**, 214–216 (1989). <https://link.aps.org/doi/10.1103/PhysRevLett.62.214>.

[26] Fischer, O., Kugler, M., Maggio-Aprile, I., Berthod, C. & Renner, C. Scanning tunneling spectroscopy of high-temperature superconductors. *Rev. Mod. Phys.* **79**, 353–419 (2007). <https://link.aps.org/doi/10.1103/RevModPhys.79.353>.

[27] Suderow, H., Guillamón, I., Rodrigo, J. G. & Vieira, S. Imaging superconducting vortex cores and lattices with a scanning tunneling microscope. *Superconductor Science and Technology* **27**, 063001 (2014). <https://dx.doi.org/10.1088/0953-2048/27/6/063001>.

[28] Guillamón, I. *et al.* Direct observation of melting in a two-dimensional superconducting vortex lattice. *Nature Physics* **5**, 651–655 (2009). <https://doi.org/10.1038/nphys1368>.

[29] Guillamón, I. *et al.* Enhancement of long-range correlations in a 2D vortex lattice by an incommensurate 1D disorder potential. *Nature Physics* **10**, 851–856 (2014).

<https://doi.org/10.1038/nphys3132>.

[30] Duhan, R., Sengupta, S., Jesudasan, J., Basistha, S. & Raychaudhuri, P. Inverse melting and re-entrant transformations of the vortex lattice in amorphous Re_6Zr thin film. *Nature Communications* **16**, 2100 (2025). <https://doi.org/10.1038/s41467-025-57431-3>.

[31] Roy, I. *et al.* Melting of the vortex lattice through intermediate hexatic fluid in an a -MoGe thin film. *Phys. Rev. Lett.* **122**, 047001 (2019). <https://link.aps.org/doi/10.1103/PhysRevLett.122.047001>.

[32] Guillamón, I. *et al.* Direct observation of stress accumulation and relaxation in small bundles of superconducting vortices in tungsten thin films. *Phys. Rev. Lett.* **106**, 077001 (2011). <https://link.aps.org/doi/10.1103/PhysRevLett.106.077001>.

[33] Yazdani, A. *et al.* Observation of Kosterlitz-Thouless-type melting of the disordered vortex lattice in thin films of a -MoGe. *Phys. Rev. Lett.* **70**, 505–508 (1993). <https://link.aps.org/doi/10.1103/PhysRevLett.70.505>.

[34] Berghuis, P., van der Slot, A. L. F. & Kes, P. H. Dislocation-mediated vortex-lattice melting in thin films of a -Nb₃Ge. *Phys. Rev. Lett.* **65**, 2583–2586 (1990). <https://link.aps.org/doi/10.1103/PhysRevLett.65.2583>.

[35] Dasgupta, C. & Valls, O. T. Two-step melting of the vortex solid in layered superconductors with random columnar pins. *Phys. Rev. Lett.* **91**, 127002 (2003). <https://link.aps.org/doi/10.1103/PhysRevLett.91.127002>.

[36] Marchevsky, M., Keurentjes, A., Aarts, J. & Kes, P. H. Elastic deformations in field-cooled vortex lattices in NbSe₂. *Phys. Rev. B* **57**, 6061–6066 (1998). <https://link.aps.org/doi/10.1103/PhysRevB.57.6061>.

[37] Hecher, J., Zehetmayer, M. & Weber, H. W. How the macroscopic current correlates with the microscopic flux-line distribution in a type-II superconductor: an experimental study. *Superconductor Science and Technology* **27**, 075004 (2014). <https://doi.org/10.1088/0953-2048/27/7/075004>.

[38] Zehetmayer, M. How the vortex lattice of a superconductor becomes disordered: a study by scanning tunneling spectroscopy. *Scientific Reports* **5**, 9244 (2015). <https://doi.org/10.1038/srep09244>.

[39] Petrović, A. P. *et al.* Real-space vortex glass imaging and the vortex phase diagram of SnMo₆S₈. *Phys. Rev. Lett.* **103**, 257001 (2009). <https://link.aps.org/doi/10.1103/PhysRevLett.103.257001>.

[40] Empon, L. *et al.* Imaging of super-fast dynamics and flow instabilities of superconducting vortices. *Nature Communications* **8**, 85 (2017). <https://doi.org/10.1038/s41467-017-00089-3>.

[41] Bossoni, L., Carretta, P. & Poggio, M. Vortex lattice melting of a NbSe₂ single grain probed by ultrasensitive cantilever magnetometry. *Applied Physics Letters* **104**, 182601 (2014). <https://doi.org/10.1063/1.4874979>.

[42] Shibata, K., Nishizaki, T., Maki, M. & Kobayashi, N. Vortex matter in YBa₂Cu₃O_y single crystals investigated by scanning tunneling spectroscopy. *Phys. Rev. B* **72**, 014525 (2005). <https://link.aps.org/doi/10.1103/PhysRevB.72.014525>.

[43] Pan, S. H. *et al.* STM studies of the electronic structure of vortex cores in Bi₂Sr₂CaCu₂O_{8+δ}. *Phys. Rev. Lett.* **85**, 1536–1539 (2000). <https://link.aps.org/doi/10.1103/PhysRevLett.85.1536>.

[44] Yoshizawa, S. *et al.* High-resolution scanning tunneling spectroscopy of vortex cores in inhomogeneous electronic states of Bi₂Sr₂CaCu₂O_x. *Journal of the Physical Society of Japan* **82**, 083706 (2013). <https://doi.org/10.7566/JPSJ.82.083706>.

[45] Edkins, S. D. *et al.* Magnetic field-induced pair density wave state in the cuprate vortex halo. *Science* **364**, 976–980 (2019). <https://www.science.org/doi/abs/10.1126/science.aat1773>.

[46] Maggio-Aprile, I., Renner, C., Erb, A., Walker, E. & Fischer, O. Direct vortex lattice imaging and tunneling spectroscopy of flux lines on YBa₂Cu₃O₇. *Phys. Rev. Lett.* **75**, 2754–2757 (1995). <https://link.aps.org/doi/10.1103/PhysRevLett.75.2754>.

[47] Iyo, A. *et al.* New-structure-type Fe-based superconductors: CaAF₄As₄ (A=K, Rb, Cs) and SrAF₄As₄ (A=Rb, Cs). *Journal of the American Chemical Society* **138**, 3410–3415 (2016). <https://doi.org/10.1021/jacs.5b12571>. PMID: 26943024.

[48] Meier, W. R. *et al.* Anisotropic thermodynamic and transport properties of single-crystalline CaKFe₄As₄. *Physical Review B* **94**, 064501 (2016). <https://link.aps.org/doi/10.1103/PhysRevB.94.064501>.

[49] Cho, K. *et al.* Nodeless multiband superconductivity in stoichiometric single-crystalline CaKFe₄As₄. *Phys. Rev. B* **95**, 100502 (2017). <https://link.aps.org/doi/10.1103/PhysRevB.95.100502>.

[50] Singh, S. J. *et al.* Ultrahigh critical current densities, the vortex phase diagram, and the effect of granularity of the stoichiometric high-T_c superconductor CaKFe₄As₄. *Phys. Rev. Mater.* **2**, 074802 (2018). <https://link.aps.org/doi/10.1103/PhysRevMaterials.2.074802>.

[51] Fente, A. *et al.* Influence of multiband sign-changing superconductivity on vortex cores and vortex pinning in stoichiometric high-T_c CaKFe₄As₄. *Phys. Rev. B* **97**, 134501 (2018). <https://link.aps.org/doi/10.1103/PhysRevB.97.134501>.

[52] Ichinose, A., Pyon, S., Tamegai, T. & Ishida, S. Elucidating the origin of planar defects that enhance critical current density in CaKFe₄As₄ single crystals. *Superconductor Science and Technology* **34**, 034003 (2021). <https://doi.org/10.1088/1361-6668/abdb47>.

[53] He, T. *et al.* Direct observation of low-field vortex patterns in stoichiometric CaKFe₄As₄ single crystal. *Phys. Rev. B* **111**, 104512 (2025). <https://link.aps.org/doi/10.1103/PhysRevB.111.104512>.

[54] He, T. *et al.* Defect-induced vortex pattern variations in a CaKFe₄As₄ single crystal. *Physical Review B* **112**, 174516 (2025). <https://link.aps.org/doi/10.1103/3zm1-m2n6>.

[55] Takahashi, A. *et al.* Effects of splayed columnar defects on critical current density in CaKFe₄As₄. *Journal of Physics: Conference Series* **1590**, 012015 (2020). <https://doi.org/10.1088/1742-6596/1590/1/012015>.

[56] Kobayashi, Y., Pyon, S., Takahashi, A. & Tamegai, T. Effects of point defects introduced by Co-doping and proton irradiation in CaKFe₄As₄. *Journal of Physics: Conference Series* **1590**, 012014 (2020). <https://doi.org/10.1088/1742-6596/1590/1/012014>.

[57] Haberkorn, N. *et al.* Enhancement of critical current density in CaKFe₄As₄ single crystals through 3 MeV proton irradiation. *Superconductor Science and Technology* **33**, 025008 (2020). <https://doi.org/10.1088/0953-2048/33/2/025008>.

1361-6668/ab5f4b.

[58] Haberkorn, N. *et al.* Effect of Ni doping on vortex pinning in $\text{CaK}(\text{Fe}_{1-x}\text{Ni}_x)_4\text{As}_4$ single crystals. *Phys. Rev. B* **100**, 064524 (2019). <https://link.aps.org/doi/10.1103/PhysRevB.100.064524>.

[59] Chen, Y. *et al.* Evolution of critical current density in $\text{CaKFe}_4\text{As}_4$ with La-doping. *Superconductor Science and Technology* **38**, 015004 (2024). <https://doi.org/10.1088/1361-6668/ad8e00>.

[60] Huyan, S., Haberkorn, N., Xu, M., Canfield, P. C. & Bud'ko, S. L. Effects of pressure on superconducting properties and vortex pinning of $\text{CaKFe}_4\text{As}_4$ single crystals. *Journal of the Physical Society of Japan* **94**, 024708 (2025). <https://doi.org/10.7566/JPSJ.94.024708>.

[61] Cui, J. *et al.* Magnetic fluctuations and superconducting properties of $\text{CaKFe}_4\text{As}_4$ studied by As 75 NMR. *Physical Review B* **96**, 104512 (2017). <https://link.aps.org/doi/10.1103/PhysRevB.96.104512>.

[62] Kohen, A. *et al.* Superconducting vortex profile from fixed point measurements the “lazy fisherman” tunneling microscopy method. *Applied Physics Letters* **86**, 212503 (2005). <https://doi.org/10.1063/1.1939077>.

[63] Mou, D. *et al.* Enhancement of the superconducting gap by nesting in $\text{CaKFe}_4\text{As}_4$: A new high temperature superconductor. *Phys. Rev. Lett.* **117**, 277001 (2016). <https://link.aps.org/doi/10.1103/PhysRevLett.117.277001>.

[64] Dew-Hughes, D. Flux pinning mechanisms in type-II superconductors. *Philosophical Magazine* **30**, 293–305 (1974). <https://doi.org/10.1080/14786439808206556>.

[65] Cheng, W., Lin, H., Shen, B. & Wen, H.-H. Comparative study of vortex dynamics in $\text{CaKFe}_4\text{As}_4$ and $\text{Ba}_{0.6}\text{K}_{0.4}\text{Fe}_2\text{As}_2$ single crystals. *Science Bulletin* **64**, 81–90 (2019). <https://www.sciencedirect.com/science/article/pii/S2095927318306078>.

[66] Wang, C. *et al.* Flux pinning and the vortex phase diagram in optimized $\text{CaKFe}_4\text{As}_4$ single crystals fabricated by a one-step method. *Superconductor Science and Technology* **33**, 045011 (2020). <https://doi.org/10.1088/1361-6668/ab75aa>.

[67] Wang, C. *et al.* Vortex creep activation energies and depinning currents in $\text{CaKFe}_4\text{As}_4$ and $\text{Ba}_{0.6}\text{K}_{0.4}\text{Fe}_2\text{As}_2$ revealed by AC susceptibility measurements. *Journal of Physics: Condensed Matter* **32**, 415607 (2020). <https://doi.org/10.1088/1361-648X/ab9f50>.

[68] Ishida, S. *et al.* Unique defect structure and advantageous vortex pinning properties in superconducting $\text{CaKFe}_4\text{As}_4$. *npj Quantum Materials* **4**, 27 (2019). <https://doi.org/10.1038/s41535-019-0165-0>.

[69] Pyon, S. *et al.* Large and significantly anisotropic critical current density induced by planar defects in $\text{CaKFe}_4\text{As}_4$ single crystals. *Phys. Rev. B* **99**, 104506 (2019). <https://link.aps.org/doi/10.1103/PhysRevB.99.104506>.

[70] Daeumling, M., Seuntjens, J. M. & Larbalestier, D. C. Oxygen-defect flux pinning, anomalous magnetization and intra-grain granularity in $\text{YBa}_2\text{Cu}_3\text{O}_{7-\delta}$. *Nature* **346**, 332–335 (1990). <https://doi.org/10.1038/346332a0>.

[71] Yang, H., Luo, H., Wang, Z. & Wen, H.-H. Fishtail effect and the vortex phase diagram of single crystal $\text{Ba}_{0.6}\text{K}_{0.4}\text{Fe}_2\text{As}_2$. *Applied Physics Letters* **93**, 142506 (2008). <https://doi.org/10.1063/1.2996576>.

[72] Taen, T., Tsuchiya, Y., Nakajima, Y. & Tamegai, T. Superconductivity at $T_c \sim 14$ K in single-crystalline $\text{FeTe}_{0.61}\text{Se}_{0.39}$. *Phys. Rev. B* **80**, 092502 (2009). <https://link.aps.org/doi/10.1103/PhysRevB.80.092502>.

[73] Prozorov, R. *et al.* Vortex phase diagram of $\text{Ba}(\text{Fe}_{0.93}\text{Co}_{0.07})_2\text{As}_2$ single crystals. *Phys. Rev. B* **78**, 224506 (2008). <https://link.aps.org/doi/10.1103/PhysRevB.78.224506>.

[74] Prozorov, R. *et al.* Magneto-optical study of $\text{Ba}(\text{Fe}_{1-x}\text{M}_x)_2\text{As}_2$ ($M = \text{Co}$ and Ni) single crystals irradiated with heavy ions. *Phys. Rev. B* **81**, 094509 (2010). <https://link.aps.org/doi/10.1103/PhysRevB.81.094509>.

[75] Prommapan, P. *et al.* Magnetic-field-dependent pinning potential in LiFeAs superconductor from its Campbell penetration depth. *Phys. Rev. B* **84**, 060509 (2011). <https://link.aps.org/doi/10.1103/PhysRevB.84.060509>.

[76] Prozorov, R. *et al.* Doping – dependent irreversible magnetic properties of $\text{Ba}(\text{Fe}_{1-x}\text{Co}_x)_2\text{As}_2$ single crystals. *Physica C: Superconductivity* **469**, 667–673 (2009). <https://www.sciencedirect.com/science/article/pii/S0921453409001063>. Superconductivity in Iron-Pnictides.

[77] Sugali, P. K. N. *et al.* Intrinsic defect structures of polycrystalline $\text{CaKFe}_4\text{As}_4$ superconductors. *Phys. Chem. Chem. Phys.* **23**, 19827–19833 (2021). <http://dx.doi.org/10.1039/D1CP02613E>.

[78] Haberkorn, N., Suárez, S., Bud'ko, S. L. & Canfield, P. C. Strong pinning and slow flux creep relaxation in Co-doped CaFe_2As_2 single crystals. *Solid State Communications* **318**, 113963 (2020). <https://www.sciencedirect.com/science/article/pii/S0038109820304695>.

[79] Eskildsen, M. R. *et al.* Structural stability of the square flux line lattice in $\text{YNi}_2\text{B}_2\text{C}$ and $\text{LuNi}_2\text{B}_2\text{C}$ studied with small angle neutron scattering. *Phys. Rev. Lett.* **79**, 487–490 (1997). <https://link.aps.org/doi/10.1103/PhysRevLett.79.487>.

[80] Densmore, J. M. *et al.* Small-angle neutron scattering study of the vortex lattice in superconducting $\text{LuNi}_2\text{B}_2\text{C}$. *Phys. Rev. B* **79**, 174522 (2009). <https://link.aps.org/doi/10.1103/PhysRevB.79.174522>.

[81] Yaron, U. *et al.* Microscopic coexistence of magnetism and superconductivity in $\text{ErNi}_2\text{B}_2\text{C}$. *Nature* **382**, 236–238 (1996). <https://doi.org/10.1038/382236a0>.

[82] Miranović, P. & Kogan, V. G. Elastic moduli of vortex lattices within nonlocal London model. *Phys. Rev. Lett.* **87**, 137002 (2001). <https://link.aps.org/doi/10.1103/PhysRevLett.87.137002>.

[83] Wu, H., Wang, Y. & Ali, M. N. The global critical current effect of superconductivity (2024). <https://arxiv.org/abs/2412.20896>. 2412.20896.

[84] Park, J. M., Sun, S., Watanabe, K., Taniguchi, T. & Jarillo-Herrero, P. Experimental evidence for nodal superconducting gap in moiré graphene. *Science* **391**, 79–83 (2025). <https://www.science.org/doi/abs/10.1126/science.adv8376>.

[85] Navarro-Moratalla, E. *et al.* Enhanced superconductivity in atomically thin TaS_2 . *Nature Communications* **7**, 11043 (2016). <https://doi.org/10.1038/ncomms11043>.

[86] Fridman, N. *et al.* Anomalous thickness dependence of the vortex pearl length in few-layer NbSe_2 . *Nature*

Communications **16**, 2696 (2025). <https://doi.org/10.1038/s41467-025-57817-3>.

[87] Córdoba, R. *et al.* 3D superconducting hollow nanowires with tailored diameters grown by focused He⁺ beam direct writing. *Beilstein Journal of Nanotechnology* **11**, 1198–1206 (2020). <https://doi.org/10.3762/bjnano.11.104>.

[88] Meier, W. R., Kong, T., Bud'ko, S. L. & Canfield, P. C. Optimization of the crystal growth of the superconductor CaKFe₄As₄ from solution in the FeAs-CaFe₂As₂-KFe₂As₂. *Phys. Rev. Mater.* **1**, 013401 (2017). <https://link.aps.org/doi/10.1103/PhysRevMaterials.1.013401>.

[89] Suderow, H., Guillamón, I. & Vieira, S. Compact very low temperature scanning tunneling microscope with mechanically driven horizontal linear positioning stage. *Review of Scientific Instruments* **82**, 033711 (2011). <https://doi.org/10.1063/1.3567008>.

[90] Rodrigo, J., Suderow, H., Vieira, S., Bascones, E. & Guinea, F. Superconducting nanostructures fabricated with the scanning tunnelling microscope. *Journal of Physics: Condensed Matter* **16**, R1151 (2004). <https://iopscience.iop.org/article/10.1088/0953-8984/16/34/R01>.

[91] Martín-Vega, F. *et al.* Simplified feedback control system for scanning tunneling microscopy. *Review of Scientific Instruments* **92**, 103705 (2021). <https://doi.org/10.1063/5.0064511>.

[92] LowTemperaturesUAM. <https://github.com/LowTemperaturesUAM> (2025). GitHub.

[93] Horcas, I. *et al.* WSXM: A software for scanning probe microscopy and a tool for nanotechnology. *Review of Scientific Instruments* **78**, 013705 (2007). <https://doi.org/10.1063/1.2432410>.

[94] Montoya, R. Á. *et al.* Methods to simplify cooling of liquid helium cryostats. *HardwareX* **5** (2019). <https://doi.org/10.1016/j.hwx.2019.e00058>.

[95] Llorens, J. B. *et al.* Observation of a gel of quantum vortices in a superconductor at very low magnetic fields. *Phys. Rev. Res.* **2**, 013329 (2020). <https://link.aps.org/doi/10.1103/PhysRevResearch.2.013329>.

[96] Herrera, E. *et al.* Vortex creep at very low temperatures in single crystals of the extreme type-II superconductor Rh₉In₄S₄. *Phys. Rev. B* **95**, 134505 (2017). <https://link.aps.org/doi/10.1103/PhysRevB.95.134505>.

[97] Willa, R. *et al.* Thermal creep induced by cooling a superconducting vortex lattice. *Phys. Rev. Res.* **2**, 013125 (2020). <https://link.aps.org/doi/10.1103/PhysRevResearch.2.013125>.

[98] Cao, L. *et al.* The As-surface of an iron-based superconductor CaKFe₄As₄. *Nano Research* **14**, 3921–3925 (2021). <https://doi.org/10.1007/s12274-021-3316-0>.

[99] Stolyarov, V. S. *et al.* Domain meissner state and spontaneous vortex-antivortex generation in the ferromagnetic superconductor EuFe₂(As_{0.79}P_{0.21})₂. *Science Advances* **4**, eaat1061 (2018). <https://www.science.org/doi/abs/10.1126/sciadv.aat1061>.

[100] Wang, Z. *et al.* Evidence for dispersing 1D Majorana channels in an iron-based superconductor. *Science* **367**, 104–108 (2020). <https://www.science.org/doi/abs/10.1126/science.aaw8419>.

[101] Mesaros, A., Gu, G. D. & Massei, F. Topologically trivial gap-filling in superconducting Fe(Se,Te) by one-dimensional defects. *Nature Communications* **15**, 3774 (2024). <https://doi.org/10.1038/s41467-024-48047-0>.

[102] Herrera, E. *et al.* Quantum-well states at the surface of a heavy-fermion superconductor. *Nature* **616**, 465–469 (2023). <https://doi.org/10.1038/s41586-023-05830-1>.

[103] Wang, C. *et al.* Novel sample-thickness-dependent flux pinning behaviors of KFe₂As₂ intercalations in CaKFe₄As₄ single crystals. *Superconductor Science and Technology* **34**, 055001 (2021). <https://doi.org/10.1088/1361-6668/abecd0>.

[104] Springholz, G. Strain contrast in scanning tunneling microscopy imaging of subsurface dislocations in lattice-mismatched heteroepitaxy. *Applied Surface Science* **112**, 12–22 (1997). <https://www.sciencedirect.com/science/article/pii/S0169433296009993>.

[105] Fente, A. *et al.* Field dependence of the vortex core size probed by scanning tunneling microscopy. *Phys. Rev. B* **94**, 014517 (2016). <https://link.aps.org/doi/10.1103/PhysRevB.94.014517>.

[106] Kogan, V. G. & Zhelezina, N. V. Field dependence of the vortex core size. *Phys. Rev. B* **71**, 134505 (2005). <https://link.aps.org/doi/10.1103/PhysRevB.71.134505>.

[107] Willa, R., Geshkenbein, V. B. & Blatter, G. Hessian characterization of the pinning landscape in a type-II superconductor. *Phys. Rev. B* **105**, 144504 (2022). <https://link.aps.org/doi/10.1103/PhysRevB.105.144504>.

[108] Buchacek, M., Geshkenbein, V. B. & Blatter, G. Role of rare events in the pinning problem. *Phys. Rev. Res.* **2**, 043266 (2020). <https://link.aps.org/doi/10.1103/PhysRevResearch.2.043266>.